Material Matters™

Volume 8, Number 4

ALDRICH Materials Science

Materials for Energy Storage and Efficiency

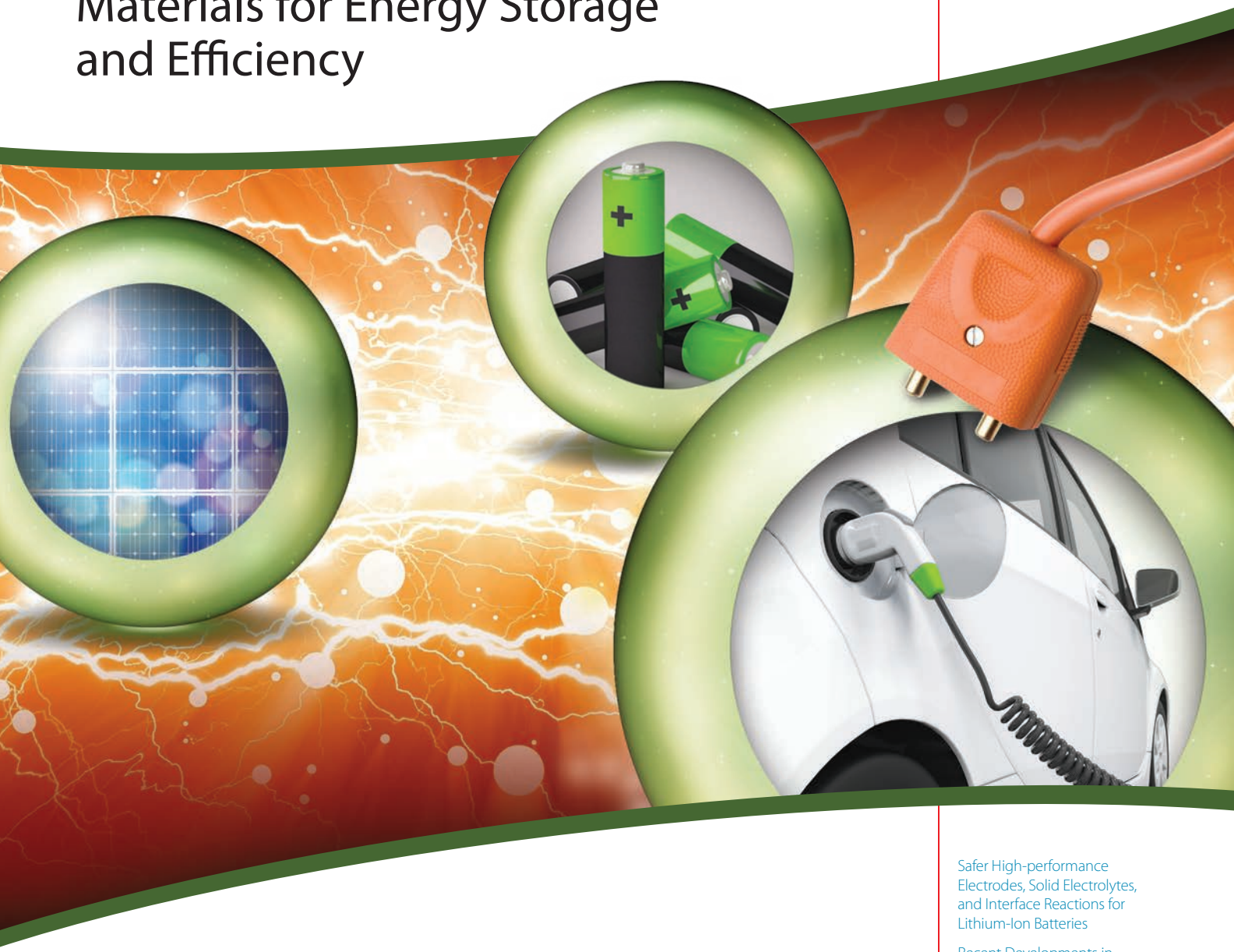

Energizing Innovation

SIGMA-ALDRICH®

Introduction

Meenakshi Hardi, Ph.D.
Aldrich Materials Science

Welcome to the fourth issue of ***Material Matters™*** for 2013 focusing on *Materials for Energy Storage and Efficiency*. Energy is vital for economic growth. Since the industrial revolution, fossil fuels have served as the major energy source powering the growth of our economy and society. However, increasing global energy demand, coupled with finite supply and long-term environmental effects, means alternative energy sources must provide a larger portion of the energy mix. Alternative energy sources include those that are renewable and environmentally clean, such as solar power, hydrogen-based energy, biofuels, wind, hydroelectric, and geothermal energy. In order for alternative energy to become a major contributor to the global energy supply, however, two significant challenges must be overcome. First, the efficiency of energy generation must improve to the extent that it is at least competitive with existing fossil fuels. Second, lightweight and high-performance storage devices will be required both for mobility and to compensate for the intermittency of power sources such as wind and solar energy generation.

Over the last few years, lithium-ion batteries have emerged as one of the most promising energy storage devices due to their high energy density storage capacity. Li-ion batteries are widely used in portable electronics; and currently, numerous research efforts are focused on their large-scale implementation in hybrid and pure electric vehicles. However, these large-scale transportation applications are primarily hindered by performance, safety, and cost of the electrode, electrolyte materials, and other battery components.

In our first article, Professors Yves Chabal, Kyeongjae Cho and Christopher Hinkle (USA) discuss certain classes of materials for next-generation cathodes and solid electrolytes that promise new benchmarks for safety and affordability. This article also shows how advanced chemical spectroscopy and first principles modeling can be utilized to study the interface reactions between the new electrode and electrolyte materials to improve battery performance and stability.

In the second article, Professors Xuefeng Song and Lian Gao (China) review the next generation of anode materials designed to meet the high energy demands of Li-ion batteries for the hybrid and electric automobile market. The article focuses on silicon as a promising replacement material for graphite anodes. Advantages of silicon anodes include high theoretical capacity and relatively low working potential, as well as low cost and toxicity. The authors also describe several viable solutions to the problem of volumetric change encountered during the charge/discharge cycle that is commonly observed when Si anodes are used in Li-ion batteries.

Professor Kessels (Netherlands), in the third article, describes how nanomaterials can improve performance and enable large-scale implementation of alternative energy technologies. Many challenges arise when building devices from nanomaterials, particularly in the preparation, modification, functionalization, and stabilization of nanomaterials for large-scale applications. In this micro-review, atomic layer deposition (ALD) is shown, through examples, as a scalable solution for fabrication of high-performance nanomaterials including thin films and nanostructured materials for different energy applications, such as Li-ion batteries, fuel cells, and solar cells.

Finally, Professor Nam-Gyu Park (South Korea) reviews recent advances in the use of nanoscale inorganic light harvesters and sensitizers to improve the efficiency and performance of dye-sensitized solar cells. Inorganic sensitizers such as metal chalcogenides and organometal halide perovskites are considered as promising new routes to construct low-cost high efficiency solar cells. Additionally, quantum dots are also reviewed as promising sensitizers to further improve the efficiency of solar cells. High absorption coefficients, tunable band gaps, the ability to absorb light from visible to IR region, and the possibility of multiple exciton generation (MEG) are highlighted.

Each article is accompanied by a list of relevant materials available from Aldrich® Materials Science. For additional product information, visit us at aldrich.com/matsci. Send your comments or suggestions for ***Material Matters™*** or your product suggestions to matsci@sial.com.

About Our Cover

Advancements in alternative energy technologies along with adjacent areas of energy conversion, storage and efficiency are essential for securing our energy future. The cover art of this issue represents examples of a few energy conversion and storage devices such as solar cells and batteries addressing the global energy demands. Aldrich Materials Science is proud to help enable these alternative energy technologies with a large variety of innovative materials.

Material Matters™

Vol. 8, No. 4

Aldrich Materials Science
Sigma-Aldrich Co. LLC
6000 N. Teutonia Ave.
Milwaukee, WI 53209, USA

To Place Orders

Telephone	800-325-3010 (USA)
FAX	800-325-5052 (USA)

International customers, contact your local Sigma-Aldrich office (sigma-aldrich.com/worldwide-offices).

Customer & Technical Services

Customer Inquiries	800-325-3010
Technical Service	800-325-5832
SAFC®	800-244-1173
Custom Synthesis	800-244-1173
Flavors & Fragrances	800-227-4563
International	314-771-5765
24-Hour Emergency	314-776-6555
Safety Information	sigma-aldrich.com/safetycenter
Website	sigma-aldrich.com
Email	aldrich@sial.com

Subscriptions

Request your **FREE** subscription to *Material Matters*:

Phone	800-325-3010 (USA)
Mail	Attn: Marketing Communications Aldrich Chemical Co., Inc Sigma-Aldrich Co. LLC P.O. Box 2060 Milwaukee, WI 53201-2060
Website	aldrich.com/mm
Email	sams-usa@sial.com

Material Matters (ISSN 1933–9631) is a publication of Aldrich Chemical Co., Inc. Aldrich is a member of the Sigma-Aldrich Group.

Online Versions

Explore previous editions of *Material Matters*. Visit aldrich.com/materialmatters

Table of Contents

Articles

Featured Products

Your Materials Matter

Bryce P. Nelson, Ph.D.
Aldrich Materials Science Initiative Lead

We welcome fresh product ideas. Do you have a material or compound you wish to see featured in the Aldrich® Materials Science line? If it is needed to accelerate your research, it matters. Send your suggestion to ***matsci@sial.com*** *for consideration.*

Dr. Anke Weidenkaff of the EMPA-Swiss Federal Laboratories for Materials Science and Technology, Switzerland, recommended the addition of high purity Calcium Cobalt Oxide (Aldrich Prod. No. 791032) to our catalog as a material for thermoelectric applications.[1] $Ca_3Co_4O_9$ (CCO) along with many other oxides are currently considered to have the most potential of all thermoelectric materials owing to its low cost, nontoxicity, light weight, high thermal and chemical stability and oxidation resistance at high temperatures.[2] CCO belongs to the family of misfit-layered oxides with one of the highest thermoelectric figures of merit (*ZT*) for the oxides. The thermoelectric power of CCO can be further improved by doping with other elements.[3,4]

References

(1) Karvonen, L; Tomeš, P, Weidenkaff, A.; *Material Matters* **2012**, *2*, 92.
(2) Koumoto, K.; Terasaki, I.; Funahashi, R.; *MRS Bulletin* **2006**, *31(3)*, 206.
(3) Xu, G.; Funahashi, R.; Shikano, M.; Matsubara, I.; Zhou, Y.; *Applied Physics Letters* **2002**, *80(20)*, 3760.
(4) Tian, R.; Donelson, R.; Ling, C. D.; Blanchard, P. E. R.; Zhang, T.; Chu, D.; Tan, T. T.; Li, S.; *J. Phys. Chem. C* **2013**, *117(26)*, 13382.

Calcium cobalt oxide

[12514-78-2] $Ca_3Co_4O_9$ FW: 499.96

Powder, ≥99.9% trace metals basis

791032	25g

Safer High-performance Electrodes, Solid Electrolytes, and Interface Reactions for Lithium-Ion Batteries



Yves J. Chabal, Kyeongjae Cho, and Christopher L. Hinkle*
(Roberto C. Longo, K. C. Santosh, Amandeep K. Sra, David E. Arreaga-Salas, and Katy Roodenko; not pictured)
Department of Materials Science and Engineering,
University of Texas at Dallas, Richardson, Texas 75082 USA
*Email: chris.hinkle@utdallas.edu

Introduction

Li-ion batteries are currently the focus of numerous research efforts with applications designed to reduce carbon-based emissions and improve energy storage capabilities.[1,2] The potential for high energy density storage capacity makes Li-ion batteries extremely promising devices for large-scale implementation in hybrid or pure electric vehicles, and in energy storage of both solar and wind power.[3,4] Li-ion batteries store chemical energy, delivering it in the form of electric power with high efficiency and no exhaust emissions.[5] They are widely used in portable electronics, but their implementation into larger-scale applications is hindered by the performance of the electrode materials and the electrolyte.[1,5,6]

Safety is also a major concern in Li-ion battery technologies, and many high profile examples of runaway reactions have the community searching for advanced materials with better stability. Typical cathode materials, such as the layered oxides ($LiMO_2$), exhibit a non-negligible instability at the end of the charging process and decompose at high temperatures. Most commercially available electrolytes, organic liquid solvents combined with a Li salt, show a remarkably high instability with respect to the release of oxygen from the cathode. To overcome these safety concerns, alternative materials systems are under intense investigation to enhance safety (nonflammable if short-circuited) and chemical stability over a wide range of ambient and operating temperatures.[7,8]

In this article, we highlight certain classes of materials for next-generation cathodes and solid electrolytes and point to interface reactions as one of the main roadblocks requiring advanced chemical spectroscopy and first-principles modeling to improve battery performance and stability.

Silicate-based Cathodes

In an effort to develop more stable and safe cathode materials, research has been focused on Fe olivine phosphate, $LiFePO_4$ (Aldrich Prod. No. 759546), which was proposed as a cathode material in 1997.[1] Olivine structures are attractive mainly because they are non-toxic, potentially inexpensive, and remarkably stable due to the strength of the oxyanion group (PO_4), even under harsh operating conditions.[2,3] Moreover, recent results in nanostructuring and carbon-coating $LiFePO_4$ particles have noticeably improved their performance, with a demonstrated rate capability and cyclability close to a commercially acceptable level.[3] However, low energy density (the equilibrium potential is only ~3.4 V) and relatively low ionic and electronic conductivities represent major hurdles for use in applications where high energy and power densities are required (such as hybrid electric vehicles).[1]

Considering the potential for polyoxyanion compounds as safe and cheap cathode materials, the silicates constitute an interesting alternative to phosphates.[4,5] The Si–O bond is at least as stable as any other polyoxyanion group, yielding the necessary thermal stability for medium- and large-scale energy applications. Moreover, a newly synthesized family of compounds belonging to the family of the orthosilicates, Li_2MSiO_4 (M = transition metals such as Fe, Mn, and/or Ni), shows the interesting possibility of extracting two Li atoms per Li_2MSiO_4 in two consecutive redox processes, allowing a potential capacity (330 mAh/g) almost twice that of current cathode materials.[5] However, this extraction of two Li atoms per formula unit has yet to be demonstrated experimentally due to a number of issues.[5] Some practical problems are the high voltage at which the extraction of the second electron in Li_2FeSiO_4 occurs, the low electronic conductivity of these medium-gap insulators, and the low ionic conductivity which is comparable to the Fe phosphates.[5] An additional significant challenge is structural stability as this tetrahedral family of compounds has several different morphologies with similar formation energies,[5] and a phase transformation after the first cycle of charge/discharge has been reported. All of these shortcomings must be addressed in order to achieve the full potential of the silicates.[5]

In a strategy that was originally applied to improve the performance of layered oxides and olivine phosphates,[6] additional transition metals were introduced in the silicate cathode material to overcome some of the aforementioned problems. **Figure 1** shows our calculated voltages, using first-principles density-functional theory (DFT) calculations, of the two electron redox processes for different silicate polymorphs and different transition metal compositions. These calculations suggest several important features that should lead to improved silicate design. First, the operational voltage dependence on the transition metal species is stronger than the operational voltage dependence on the different polymorphs. Second, for the initial electron redox process, the voltage increases with the amount of secondary transition metal "doping" concentration (for example, going from $Fe_{0.75}Mn_{0.25}$ to $Fe_{0.5}Mn_{0.5}$) while the voltage of a ternary distribution of transition metal cations (Fe-Mn-Ni) with 33% stoichiometry is somewhere in between. Third, the voltage during the first Li extraction also increases with the number of electrons in the outer *d*-shell as expected.[4] For the crucial second electron redox process, the voltage trend is opposite to that of the first redox process, decreasing with the increased secondary transition metal concentration and number of *d*-shell electrons. The voltages range from 3.43 V ($Li_2Mn_{0.25}Fe_{0.75}SiO_4$, $Pmn2_1$ polymorph) to 4.34 V ($Li_2Ni_{0.5}Fe_{0.5}SiO_4$, $Pmn2_1$ polymorph) for the first electron process and from 5.3 V ($Li_2Mn_{0.25}Fe_{0.75}SiO_4$, $Pmn2_1$ polymorph) to 4.13 V ($Li_2Mn_{0.33}Fe_{0.33}Ni_{0.33}SiO_4$, $P2_1/n$ polymorph) for the second electron process.

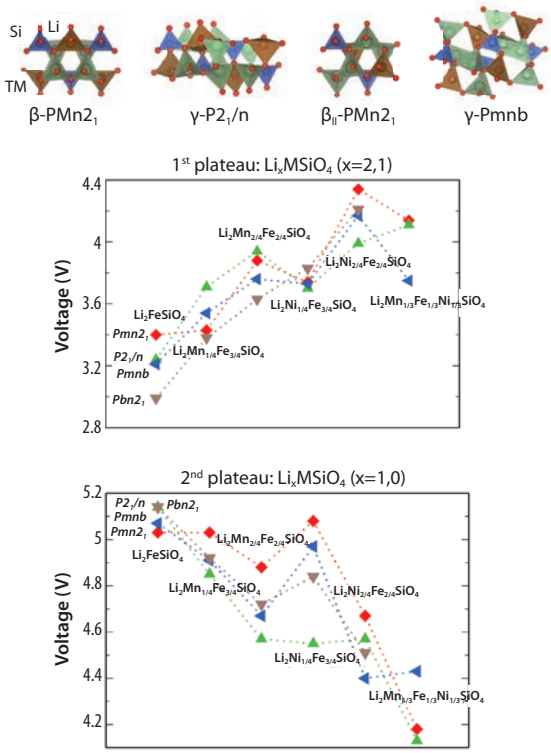

Figure 1. Structure of different silicate polymorphs. Redox potentials of the two plateaus of Li extraction from doped Li_2TMSiO_4.

All the multicomponent silicates studied have a negative formation energy, meaning they are all thermodynamically stable at room temperature. The structural distortion induced by a multicomponent transition metal cation solid solution decreases the relative stability of the $LiMSiO_4$ intermediate compound (formation energy), thus increasing the first plateau of the operating voltage while *decreasing* the second plateau (corresponding to the fully de-lithiated second electron redox process). These operating voltages are easily achievable within conventional Li-ion batteries. The addition of Mn and Ni doping impurities decreases the cationic repulsion that appears during the extraction of Li, implying each of the polymorphs is more stable with respect to the two-electron redox process of the pure Fe silicates. This stability increases the rate capability of these compounds by dropping the voltage step between the first and second Li extraction processes. Additionally, the inclusion of Ni reduces the band gap of the silicate, increasing the electronic conductivity while our calculations show the presence of Fe-related, localized, non-hybridized *d*-states that may further enhance electronic conductivity through polaronic mechanisms. All of these findings point to the use of multicomponent tetrahedral silicates to improve cathode performance. Unfortunately, the problem of the phase change during de-lithiation remains unsolved.

Experimental trials have already been attempted. A mixed solid solution of $Li_2Fe_{0.5}Mn_{0.5}SiO_4$ seems promising, and higher Mn content ($Li_2Fe_{0.1}Mn_{0.9}SiO_4$) produces a stable and repeatable phase with the Mn^{3+} ion of the intermediate (semi-delithiated) step acting as an external "stabilizer".[7] A capacity of 214 mAh/g was reported but with significant fade during cycling. Studies on different stoichiometries ($Li_2Fe_{0.8}Mn_{0.2}SiO_4$) show good reversibility, but only due to the oxidation of Fe^{3+}, not tetravalent Fe or Mn, implying that no more than one electron was exchanged.[8]

Inorganic Solid Electrolytes

The interest in commercial applications of solid electrolytes for Li-ion batteries (including medical devices like pacemaker batteries) is due to their high electrical, chemical, and mechanical stability compared to the current liquid organic electrolytes. Solid electrolytes are better suited for safety and reliability since they are resistant to shocks and vibrations, are absent of self-discharge, eliminate thermal runaway, cycle more reliably, and can be scaled to smaller sizes than traditional liquid electrolytes.[9,10] The last three decades have seen the development of solid electrolyte materials and many electrolyte candidates have been proposed (**Figure 2**).[11-14] For example, lithium lanthanum titanates (LLTO), garnet-type zirconates (LLZO), Li_2S–P_2S_5-based glasses, and lithium phosphate oxynitride (LiPON)[8-13] have been used as a commercial solid electrolyte in thin film batteries.[8-11] However, the significantly lower ionic conductivity in currently available solid electrolytes severely limits their implementation. LiPON has an ionic conductivity of 10^{-6} S cm^{-1} while LLTO and lithium thiophosphates have ionic conductivities of the order of 10^{-3} S cm^{-1}, significantly lower than organic liquid electrolytes (10^{-2} S cm^{-1}). As in cathode materials, the use of multivalent ions in solid electrolytes facilitates higher charge transfer. However, strong electrostatic interactions between the lattice and those multivalent ions enhances ionic migration energy barriers, resulting in low ionic conductivities. In addition, the mobility and ionic radius of the mobile ions are strongly correlated, indicating the ionic species should be neither too small nor too big to fit the available lattice pathways when designing any solid electrolyte.

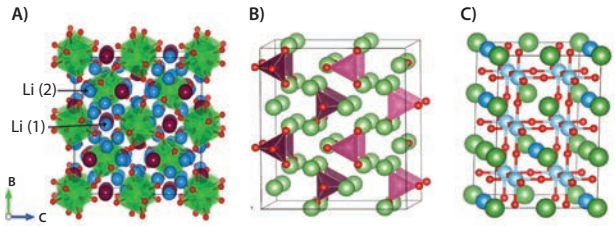

Figure 2. Atomic structures of **A)** garnet-type cubic $Li_7La_3Zr_2O_{12}$ supercell. The blue, purple, green and red balls represent Li, Zr, La and O atoms, respectively. **B)** γ-Li_3PO_4 supercell. Li atoms are indicated by green spheres, whereas the PO_4 groups are indicated by purple tetrahedra with red spheres (oxygen) at each corner. **C)** Lithium lanthanum titanates (LLTO) $Li_{0.25}La_{0.583}Ti_{0.167}O_3$. The blue, green, sky blue, and red balls represent Li, La, Ti, and O atoms, respectively. Adapted from Reference 14. Copyright 2013.

In solid electrolytes, the ionic transport originates from atomic disorder, such as vacancies and interstitial ions. Our previous work on LiPON solid electrolytes and their interface with an electrode using first-principles calculations shows Li defect conduction results from interstitial Li and depends on the Fermi-level position that can be tuned by electrode alloying,[14] i.e., the defect formation energy can be controlled by changing the Fermi level. For instance, if the E_f is within ~3 eV of the valence band maximum, Li^+ interstitial defects will be readily available due to their low formation energy (see **Figure 3**).

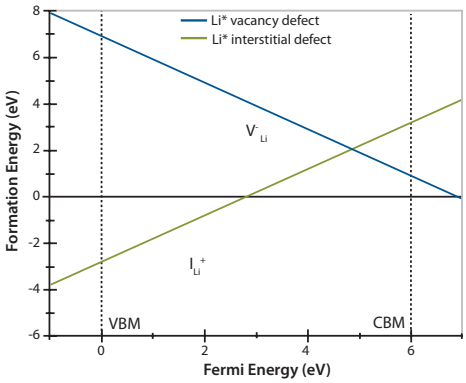

Figure 3. Li^+ defect formation energy plotted against the Fermi level across the band gap of bulk Li_3PO_4.

Conversely, the ion migration mechanism in LLTO is through Li vacancies. The partial occupancy of the Li ions contributes to the high ionic conductivity in these systems. The LLTO with the perovskite-type (ABO_3) structure (A= Li, La, or vacancy and B=Ti) has been widely investigated due to its faster Li-ion conduction (~10^{-3} S cm^{-1}) at room temperature.[12] The high ionic conductivity of Li ions is related to the low Li defect formation energy and its small Li migration barrier in hopping into neighboring A site vacancies. A similar conduction mechanism is expected in garnet-type solid electrolytes. Another advantage of LLTO is that it can also be used as a protective coating for cathode materials, enhancing the stability after the charge–discharge cycles and also for reducing the impedance of Li^+ diffusion in the composite electrode.[15] However, LLTO solid electrolytes were found to be unstable when interfacing with Li metal, whereas garnet-type solid electrolytes are found to be electrochemically stable with Li metal.

Spectroscopic Analysis of Electrode/Electrolyte Interfaces[19]

With the implementation of new materials such as silicate-based cathodes, solid electrolytes, and Si anodes (see "*Recent Developments in Silicon Anode Materials for High Performance Lithium-Ion Batteries*" in this issue), a key issue common to all of these new structures is the interface compatibility and stability.[16] Indeed, interface reactions between these and other materials critically affect their safety and performance, and therefore need to be thoroughly investigated. Here, we illustrate how advanced spectroscopic analysis can help to understand the chemical reactions and morphology progression that occurs at electrode/electrolyte interfaces, with the solid-electrolyte interphase (SEI) formation on hydrogenated amorphous Si-based anodes [using 1 M $LiPF_6$ in a 1:1 mixture of ethylene carbonate and diethyl carbonate (EC/DEC) as the electrolyte (Aldrich Prod. No. 746746)].

The SEI, formed through the decomposition of the electrolyte on the electrode surface into an insoluble solid film, is an important element of the power cyclability and cycle life of Li-ion batteries. In order to maintain repeatable lithiation reactions, the SEI layer formation must be fully understood as it controls the passivation, stability, and impedance of the electrode. Thus, it is critical to identify the composition and the mechanism of formation of the chemical species present in the SEI layer.

Several groups have reported the use of surface characterization techniques such as FTIR, Raman, and XPS to study the SEI formation on silicon anodes.[17-20] The anodes used for these studies are designed to exclude the effects of the other electrode components (binding material and conductor) on the SEI formation. Several groups have reported fabrication of binder-free electrodes such as undoped crystalline silicon (001) wafers, electrophoretic deposition of Si nanoparticles, and hydrogenated amorphous Si (a-Si:H) anodes.[19,20] A specific advantage of using a-Si:H anodes is that it is not subject to the stress experienced by crystalline-Si while undergoing amorphization upon first reaction with Li. The investigated SEI layers are typically formed on the Si electrode during cyclic voltammetry (C-V) measurements. Cyclic voltammetry provides not only insights into the lithiation/de-lithiation kinetics (**Figure 4A**), but also useful information related to the electrochemical stabilities of the electrolyte and electrodes, and the presence of any side reactions. During the C-V measurements, going from open-circuit potential (OCP) to 0.0 V, a characteristic peak is observed around 1.3–1.5 V during the first lithiation stage (**Figure 4A**), which is absent for the subsequent cycles. This corresponds to the beginning of SEI formation on the electrode surface.

Surface analysis utilizing XPS of the Si 2*p* region (**Figure 4B**), measured after the first lithiation, indicates the beginning of Si–Si bond scission and the insertion of Li and F into the a-Si:H matrix. During the first de-lithiation, the Si–Li peak and the Si–F peak intensities are significantly reduced, consistent with Li removal from the anode. After the second lithiation, the Si–Li peak broadens and its intensity increases significantly, indicating greater incorporation of Li in the electrode as compared to the first lithiation. Thus, the cyclic-voltammetry measurements correlated with XPS analysis indicate the first lithiation cycle primarily forms an SEI layer with a small amount of Li incorporated into the electrode itself while the second lithiation cycle results in significant Li insertion into the a-Si:H anode. The Raman data (**Figure 4C**) suggest the a-Si:H network is mostly preserved during the first cycle and extensive Si–Si bond breakage only takes place after several cycles.

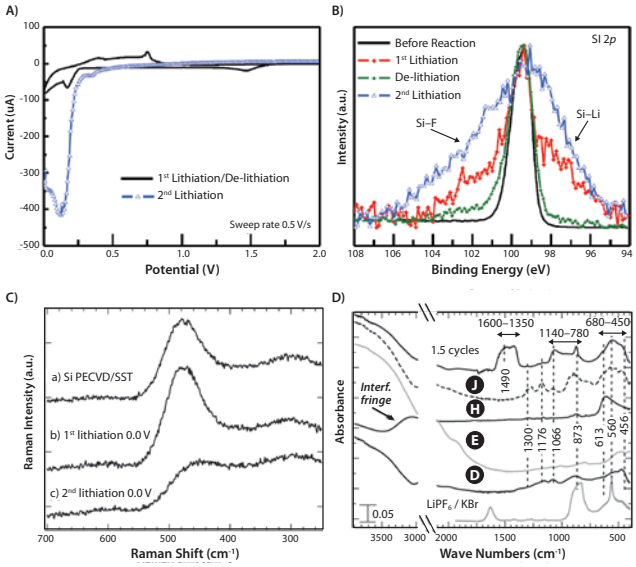

Figure 4. **A)** Cyclic-voltammetry curves of the first lithiation, first de-lithiation, and second lithiation cycles. **B)** Si 2*p* XPS spectra of the electrode at the lithiation-delithiation stages of the first and second C-V cycles. **C)** Raman data showing breakage of short-distance order caused by the insertion of significant concentrations of Li and F following the second lithiation cycle. **D)** FTIR data showing Li–F, P–F, and solvent decomposition products. Adapted from Reference 19. Copyright 2013 American Chemical Society.

The formation of an SEI layer during the first lithiation cycle can be followed by modified cyclic-voltammetry measurements. Starting from the OCP, the anodes are extracted from the cell after each voltage step of 0.2 V of the first lithiation cycle and examined by surface characterization. The intensity of the Si 2*p* peak at 99.3 eV binding energy decreases due to attenuation caused by the electrolyte decomposition and the formation of the SEI overlayer. Upon complete lithiation, the Si 2*p* peak is significantly broadened due to the insertion of Li and F into the Si matrix.

Additional evidence of chemical evolution at the interface due to decomposition of the electrolyte comes from the F 1*s* and Li 1*s* core level spectra (**Figures 5A–5B**). At an applied bias of 1.8 V, the dominant peak at 687.8 eV is due to the presence of $LiPF_6$ from the electrolyte, and the relatively smaller peak at 685.6 eV is due to the formation of LiF which is known as a main decomposition product of $LiPF_6$. Further lithiation results in a steady decrease of the $LiPF_6$ peak intensity and a concomitant *increase* in the LiF peak intensity (**Figure 5C**).

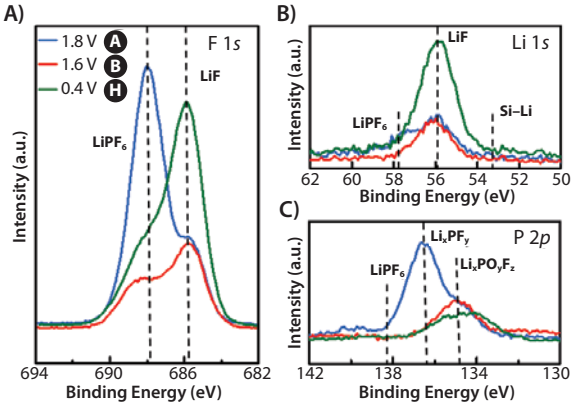

Figure 5. **A)** F 1*s* XPS spectra show the decomposition of $LiPF_6$ (at 687.8 eV) to LiF (at 685.6 eV) as the bias is applied, and in sample H (OCP to 0.4 V) the change in the slope indicates the formation of F-Si-Li_n networks. **B)** Li 1*s* XPS spectra and **C)** P 2*p* XPS spectra confirming the decomposition of $LiPF_6$ to LiF. Adapted from Reference 19. Copyright 2013 American Chemical Society.

The combination of surface analysis data leads to the following mechanism for the chemical formation of the SEI layer. During the first charging cycle at 1.8 V, the electrolyte $LiPF_6$ and the solvent begin to decompose on the electrode surface. Between 1.8–0.6 V, the decomposition of the electrolyte and solvent directly results in the formation of the SEI layer on the electrode. After the first lithiation, the SEI layer is primarily composed of LiF as the major species along with lower concentrations of the electrolyte $LiPF_6$, and the electrolyte decomposition products Li_xPF_y, and PF_y. Si does not interact with the Li and F ions until late in the first lithiation step. At biases lower than 0.4 V, the lithiation of the a-Si:H anode is initiated by the diffusion of Li and F through the SEI layer, resulting in the formation of Si–Li, Si–F, and a network of F–Si–Li_n. The initial reaction of Si with the electrolyte byproducts involves a combination of both F and Li simultaneously (not just high capacity Li–Si). These XPS results are supported by IR spectra (**Figure 4D**) showing the presence of primarily Li–F and P–F containing compounds during the first lithiation cycle. There is also absorption in a spectral range associated with Si–F bonds, in accordance with the XPS data that show the existence of Si in high oxidation states.

During the second lithiation cycle, significant scission of the Si–Si bonds by the Li occurs, resulting in the formation of high concentrations of Li_xSi. In addition, after the second lithiation cycle, the IR spectra (**Figure 4D**) contain absorption bands in the spectral range at 1,350–1,600 cm^{-1}, caused by $ROCO_2Li$, Li_2CO_3 (**Aldrich Prod. No. 752843**), and R-CO_2-M^{n+} (R=alkyl; M=Si/Li) carboxylate salts. These species correspond to typical decomposition products of carbonate-based solvents. The IR analysis indicates the SEI layer is mainly composed of organic compounds with functionalities of alkyl, carboxylate metal salt, and inorganic compounds including Li–F and P–F containing compounds.

These studies illustrate the complexity of interfacial chemistry and the need for advanced spectroscopic characterization to make progress in all aspects of electrode development. Combining this characterization with first-principles modeling and careful materials synthesis allows for the design and development of novel, safe, high-performance electrodes and electrolytes, and the controlled reactions between these new materials systems.

Acknowledgments

This manuscript was written through contributions of all authors. The authors acknowledge the full financial support of the U.S. Department of Energy, from the Office of Basic Energy Sciences, Division of Materials Sciences and Engineering under award DE-SC001951 for KR, and the Office of Energy Efficiency & Renewal Energy under award DE-EE0004186 for CH. DEA would like to thank to the Mexican Council of Science and Technology (CONACYT) for the support under the Graduate scholarship program for studies abroad. DFT calculations were performed at the Texas Advanced Computing Center (TACC).

References

(1) Padhi A. K., Nanjundaswamy K. S. and Goodenough J. B., *J. Electrochem. Soc.,* **1997**, *144*, 1188.
(2) Delacourt C., Poizot P., Morcrette M., Tarascon, J. M., Masquelier C., *Chem. Mater.,* **2004**, *16*, 93.
(3) Kang B., Ceder G., *Nature*, **2009**, *458*, 190.
(4) Larsson P., Ahuja R., Nytén A. Thomas J. O., *Electrochem. Commun.*, **2006**, *8*, 797.
(5) Islam M. S., Dominko R., Masquelier C., Sirisopanaporn C., Armstrong A. R., Bruce P. G., *J. Mater. Chem.,* **2011**, *27*, 9811.
(6) Gwon H., Seo D. H., Kim S. W., Kim J., Kang K., *Adv. Funct. Mater.,* **2009**, *19*, 3285.
(7) Kokalj A., Dominko R., Mali G., Meden A., Gaberscek M. , Jamnik J., *Chem. Mater.,* **2007**, *19*, 3633.
(8) Gong Z. L., Li Y. X., Yang Y., *Electrochem. and Sol. State Lett.,* **2006**, *9*, A542.
(9) Patil V., Shin D. W., Choi J. W., Paik D. S., Yoon S. J., *Material Research Bulletin*, **2008**, *43*, 1913.
(10) Park M., Zhang X., Chung M., Less G. B., Sastry A. M., *J. Power Sources,* **2010**, *195*, 7904.
(11) Bates J. B., Dudney N.J., Neudecker B., Ueda A., Evans C. D., *Sol. State Ionics,* **2000**, *135*, 33.
(12) Salkus T., Kazakevicius E., Kezionis A., Orliukas A. F., Badot J. C., Bohnke O., *Solid State Ionics,* **2011**, *188*, 69.
(13) Murugan R., Thangarudai V., Weppner W., Angew. *Chem., Int. Ed.* **2007**, *46*, 7778
(14) Santosh K.C., Xiong K., Longo R. C., Cho K., *J. of Power Sources,* **2013**, *244*, 136.
(15) Qian D., Xu B., Cho H. -M., Hatsukade T., Carroll K. J., Meng Y. S., *Chem. Mater.* **2012**, *24*, 2744.
(16) Chan C.K., Peng H., Liu G., McIlwrath K., Zhang X.F., Huggins R.A., Cui Y., *Nature Nanotechnology,* **2008**, *3*, 31.
(17) Philippe B., Dedryvère R., Gorgoi M., Rensmo H., Gonbeau D., Edström K., *Chem. Mater.*, 2013, *25*, 394.
(18) Nie M., Abraham D. P., Chen Y., Bose A., Lucht B. L., *J. Phys. Chem. C,* **2013**, *117 (26),* 13403.
(19) Arreaga-Salas D. E., Sra A. K., Roodenko K., Chabal Y. J. , Hinkle C. L., *J. Phys. Chem. C,* **2012**, *116* (16), 9072.
(20) Schroder K. W., Celio H., Webb L. J., Stevenson K. J., *J. Phys. Chem. C,* **2012**, *116 (37),* 19737.

Lithium-Ion Battery Materials

Electrode Sheets

For a complete list of electrode sheets, visit aldrich.com/lib.

Sheet size 5 × 10 in./80% active material on aluminum electrode substrate.

Product Name	Composition	Nominal Voltage (V)	Capacity (minimum)	Capacity (nominal)	Purity	Prod. No.
Lithium manganese nickel oxide, LMNO	$Li_2Mn_3NiO_8$	4.7 (Li/Li^+)	115 mAh/g	125 mAh/g	≥98%	765198-1EA
Lithium manganese oxide, LMO	$LiMn_2O_4$	4.7 (Li/Li^+)	110 mAh/g	120 mAh/g	≥98%	765201-1EA
Lithium nickel cobalt aluminium oxide, NCA	$LiNi_{0.8}Co_{0.15}Al_{0.05}O_2$	3.7 (Li/Li^+)	150 mAh/g	180 mAh/g	≥98%	765171-1EA
Lithium nickel manganese cobalt oxide, NMC	$LiNi_{0.33}Mn_{0.33}Co_{0.33}O_2$	3.5 (Li/Li^+)	210 mAh/g	250 mAh/g	≥99%	765163-1EA
Lithium titanate, LTO	$Li_4Ti_5O_{12}$	1.5 (Li/Li^+)	150 mAh/g	160 mAh/g	≥98%	765155-1EA

Electrolyte Solutions

For a complete list of electrolyte solutions, visit aldrich.com/lib.

Lithium Hexafluorophosphate Solutions, Battery Grade: H_2O <15 ppm; HF <50 ppm; APHA <50

Product Name	Specifications	Prod. No.
1.0 M $LiPF_6$ in EC/DMC=50/50 (v/v)	in ethylene carbonate and dimethyl carbonate	746711-100ML
1.0 M $LiPF_6$ in EC/EMC=50/50 (v/v)	in ethylene carbonate and ethyl methyl carbonate	746738-100ML
1.0 M $LiPF_6$ in EC/DEC=50/50 (v/v)	in ethylene carbonate and diethyl carbonate	746746-100ML
1.0 M $LiPF_6$ in DMC	in dimethyl carbonate	746754-100ML
1.0 M $LiPF_6$ in EMC	in ethyl methyl carbonate	746762-100ML
1.0 M $LiPF_6$ in DEC	in diethyl carbonate	746770-100ML
1.0 M $LiPF_6$ in PC	in propylene carbonate	746789-100ML

Cathode Materials

For a complete list of cathode materials, visit aldrich.com/lib.

Product Name	Composition	Description	Purity	Prod. No.
Lithium iron(II) phosphate, LFP	$LiFePO_4$	powder, >97% (XRF)	particle size <5 µm (BET)	759546-5G
Lithium cobalt phosphate, LCP	$LiCoPO_4$	powder, 99%	-	725145-25G
Lithium cobalt phosphate, LCP	$LiCoPO_4$	powder, 99.9% trace metals basis	-	777110-25G
Lithium nickel manganese cobalt oxide, NMC	$LiNi_{0.33}Mn_{0.33}Co_{0.33}O_2$	powder, >98%	particle size <0.5 µm	761001-10G
Lithium nickel cobalt aluminium oxide, NCA	$LiNi_{0.8}Co_{0.15}Al_{0.05}O_2$	powder, >98%	particle size <0.5 µm	760994-10G
Lithium manganese nickel oxide, LMNO	$Li_2Mn_3NiO_8$	powder, >99%	particle size <0.5 µm (BET)	725110-25G
Lithium nickel cobalt oxide, LNCO	$LiNi_{0.8}Co_{0.2}O_2$	powder, >98%	particle size <0.5 µm	760986-10G
Lithium manganese oxide, LMO	$LiMn_2O_4$	powder, >99%	particle size <0.5 µm (BET)	725129-25G
Lithium manganese(III,IV) oxide, LMO	$LiMn_2O_4$	-	particle size <5 µm	482277-25G
Lithium manganese dioxide	$LiMnO_2$	powder, >99% trace metals basis	particle size <1 µm	725137-25G
Lithium nickel dioxide, LNO	$LiNiO_2$	powder, ≥98% trace metals basis	particle size <3 µm (BET)	757365-10G
Lithium trivanadate, LTV	LiV_3O_8	powder, 98%	-	771511-5G
Lithium iron(III) oxide	$LiFeO_2$	powder, 95%	particle size <1 µm	442712-100G-A
Lithium cobalt(III) oxide	$LiCoO_2$	powder, 99.8% trace metals basis	-	442704-100G-A
Lithium molybdate	Li_2MoO_4	powder or crystals, 99.9% trace metals basis	-	400904-250G
Germanium(IV) sulfide	GeS_2	powder, >99.999% trace metals basis	particle size -80 mesh	756466-5G
Manganese nickel carbonate	$Mn_{0.75}Ni_{0.25}CO_3$	powder, 99.99% trace metals basis (excluding Mg)	-	763608-25G

Anode Materials

For a complete list of anode materials, visit aldrich.com/lib.

Product Name	Description	Purity	Form	Prod. No.
Lithium titanate, spinel, LTO nanopowder	particle size <200 nm (BET)	>99%	nanopowder	702277-25G
Lithium titanate, LTO	−325 mesh	-	powder	400939-100G
Lithium-aluminum alloy	-	-	powder	426490-25G
Tin(IV) oxide	particle size <100 nm (BET)	-	nanopowder	549657-5G 549657-25G
Lithium	particle size 4-10 mesh	99%, metals basis	granular	444456-10G 444456-50G
	thickness × W 1.5 × 100 mm	99.9% trace metals basis	ribbon	266000-25G 266000-100G
	thickness × W 0.75 × 45 mm	99.9% trace metals basis	ribbon	265993-25G 265993-100G
	thickness × W 0.38 × 23 mm	99.9% trace metals basis	ribbon	265985-25G 265985-100G
	diam. 3.2 mm	≥98%	wire	278327-25G 278327-100G
Graphite	particle size 200-500 nm, O.D. × I.D. × L 200-500 nm × 1-10 nm × 10-40 µm	95% trace metals basis	powder	636398-2G 636398-10G

Product Name	Description	Purity	Form	Prod. No.
Graphite	100 nm (average width, TEM) 2.5 µm (average length, TEM), D × L 50-250 nm × 0.5-5 µm	98% carbon basis	powder	698830-1G
Carbon, mesoporous	particle size <500 nm (DLS)	>99.95% trace metals basis	nanopowder	699624-5G 699624-25G
Carbon	2 - 12 µm	99.95% trace metals basis	glassy, spherical powder	484164-10G 484164-50G
Silicon	-	99.95% trace metals basis	pieces	343250-50G 343250-500G
	–60 mesh	99.999% trace metals basis	powder	267414-25G
	–325 mesh	99% trace metals basis	powder	215619-50G 215619-250G 215619-1KG
	particle size <100 nm (TEM)	≥98% trace metals basis	nanopowder	633097-10G 633097-25G

Electrolyte Materials

For a complete list of electrolyte materials, visit aldrich.com/lib.

Product Name	Composition	Purity	Form	Prod. No.
Lithium aluminum titanium phosphate, LATP	$Li_{1.3}Al_{0.3}Ti_{1.7}(PO_4)_3$	≥99.9% trace metals basis	powder	790516-10G
Lithium difluoro(oxalato)borate, LIF2OB; LIODFB; LIFOB	$LiBC_2O_4F_2$	-	powder	774138-25G
Lithium bis(oxalato)borate, LiBOB	$LiB(C_2O_4)_2$	-	powder or crystals	757136-25G
Lithium hexafluorophosphate	$LiPF_6$	≥99.99% trace metals basis	powder	450227-5G 450227-25G
Lithium trifluoromethanesulfonate, LiTf	CF_3SO_3Li	99.995% trace metals basis	powder	481548-5G 481548-25G
Lithium tetrachlorogallate	$LiGaCl_4$	99.99% trace metals basis	beads	736317-5G
Lithium tetrachloroaluminate	$LiAlCl_4$	99.99% trace metals basis	beads	451142-5G
Lithium tetrafluoroborate	$LiBF_4$	99.99% trace metals basis	powder	451622-5G 451622-25G
Lithium perchlorate	$LiClO_4$	99.99% trace metals basis	powder and chunks	634565-10G 634565-100G
Lithium hexafluoroarsenate(V)	$LiAsF_6$	98%	powder	308315-10G
Lithium phosphate monobasic	LiH_2PO_4	99%	powder or crystals	442682-500G-A

Solvents and Additives

For a complete list of solvents and additives, visit aldrich.com/lib.

Product Name	Structure	Purity	Prod. No.
Allyl methyl sulfone, MAS	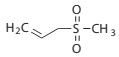	96%	718203-5G
Diethyl sulfite, DES	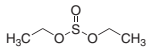	98%	774278-25G
1,5,2,4-Dioxadithiane-2,2,4,4-tetraoxide		-	774286-10G
Ethylene sulfite, ES		≥99.0%	774251-25G
Ethyl methyl carbonate, EMC	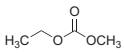	99%	754935-50ML
Fluoroethylene carbonate, FEC		99%	757349-25G
3-(Methylsulfonyl)-1-propyne	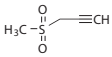	95%	718319-5G
1,2-Propyleneglycol sulfite, PS		≥98%	774456-10G
Propylene sulfate		≥99%	774294-10G
1,3-Propylene sulfite, TMS; PS		99.5%	774243-25G
Vinylene carbonate, VC		99%	757144-25G

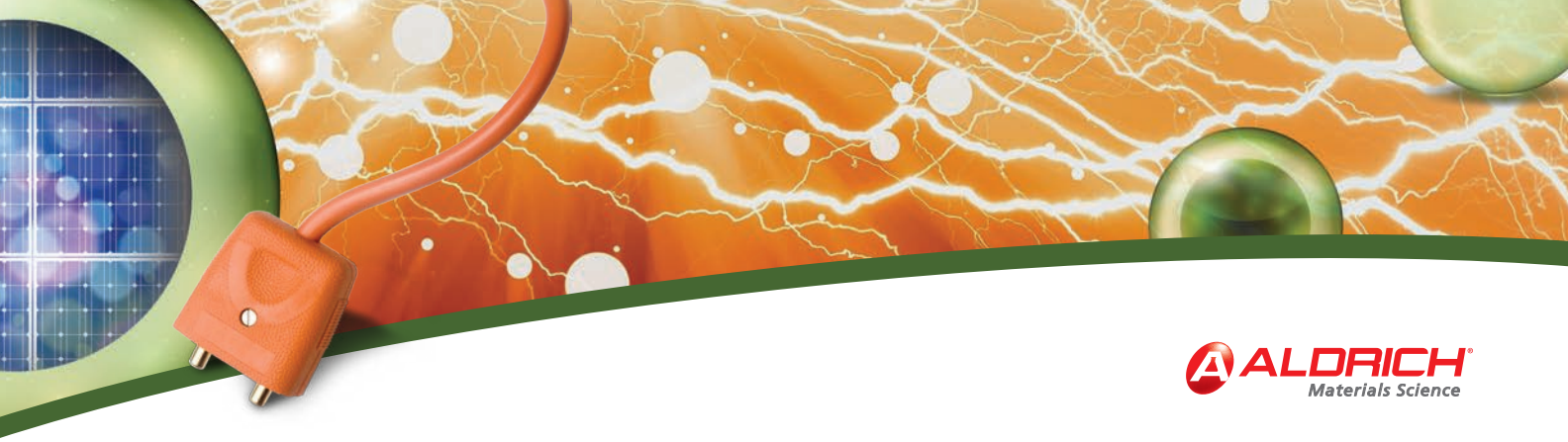

ALDRICH®
Materials Science

Anhydrous Solvents for Materials Science

Exceptionally Dry with Sure/Seal™ Bottles

Sigma-Aldrich provides the largest offering of high-quality anhydrous solvents with exceptionally low water levels. The key to our ability to provide a wide range and exceptionally dry anhydrous solvent is the Sure/Seal™ bottles and the new plug-style seals.

- Largest selection of anhydrous solvents
- Extremely low water content
- Best anhydrous quality on the market
- Aldrich® Sure/Seal™ packaging

Sure/Seal™ bottles come in a wide range of sizes: 100 mL to 2 L. Larger volumes can benefit from our Green Bulk Returnable Container program.

SIAL Prod. No.	Name	Water Specification	Available Package Sizes
310328	Propylene carbonate	≤20 ppm	100 mL, 500 mL, 1 L, 2 L
517127	Dimethyl carbonate	≤20 ppm	100 mL, 1 L, 2 L
517135	Diethyl carbonate	≤20 ppm	100 mL, 1 L
244511	Toluene	≤10 ppm	100 mL, 1 L, 2 L, 12 × 100 mL
296325	*m*-Xylene	≤20 ppm	100 mL, 1 L, 2 L, 4 × 2L
294780	*o*-Xylene	≤30 ppm	100 mL, 1 L, 2 L
296333	*p*-Xylene	≤20 ppm	100 mL, 1 L, 2 L
186562	Tetrahydrofuran, BHT inhibitor	≤20 ppm	100 mL, 1 L, 2 L, 12 × 100 mL, 6 × 1 L, 4 × 2 L
401757	Tetrahydrofuran, inhibitor free	≤20 ppm	100 mL, 1 L, 2 L, 12 × 100 mL, 6 × 1 L, 4 × 2 L
414247	2-Methyltetrahydrofuran, BHT inhibitor	≤20 ppm	100 mL, 1 L, 2 L, 12 × 100 mL, 6 × 1 L, 4 × 2 L
673277	2-Methyltetrahydrofuran, inhibitor free	≤20 ppm	100 mL, 1 L, 2 L, 12 × 100 mL
271004	Acetonitrile	≤10 ppm	100 mL, 1 L, 2 L, 12 × 100 mL, 6 × 1 L, 4 × 2 L
322415	Methanol	≤20 ppm	100 mL, 1 L, 2 L, 12 × 100 mL, 6 × 1 L, 4 × 2 L
459836	Ethanol 200 proof	≤5 ppm	100 mL, 1 L, 2 L, 12 × 100 mL, 6 × 1 L, 4 × 2 L
277649	Ethanol, denatured	≤5 ppm	100 mL, 1 L, 2 L, 12 × 100 mL, 6 × 1 L, 4 × 2 L
278475	2-Propanol	≤30 ppm	100 mL, 1 L, 2 L, 12 × 100 mL, 6 × 1 L

For more information, visit
aldrich.com/anhydrous

Recent Developments in Silicon Anode Materials for High Performance Lithium-Ion Batteries

Xuefeng Song,[1*] Xiaobing Wang,[2] Zhuang Sun,[1] Peng Zhang,[1] and Lian Gao[1]
[1]State Key Laboratory for Metallic Matrix Composite Materials,
School of Materials Science and Engineering, Shanghai Jiao Tong University,
Shanghai, 200240, China
[2]Baoshan Iron & Steel Co., Ltd. Tube, Pipe and Bar Business,
Baoshan District, Shanghai, 201900, China
*Email: songxfeng@sjtu.edu.cn

Introduction

Recent demand for electric and hybrid vehicles, coupled with a reduction in prices, has caused lithium-ion batteries (LIBs) to become an increasingly popular form of rechargeable battery technology. According to a new IHS Isuppli Rechargeable Batteries Special Report 2011, global lithium-ion battery revenue is expected to expand to $53.7 billion in 2020, up from $11.8 billion in 2010.[1] However, graphite (**Aldrich Prod. Nos. 496596, 636398,** and **698830**), the traditional anode material in lithium-ion batteries, does not meet the high energy demands of the advanced electric and hybrid automobile market due to its limited theoretical specific capacity of ~370 mAh g^{-1}.[2] This has led to the proposal of a large number of anode materials with enhanced storage capacity, high energy density, and improved cycle characteristics for lithium-ion batteries over the last decade.[3-7] **Table 1** summarizes the properties of several different anode materials. Among these advanced anode materials, Si has attracted substantial attention as an alternative for Li-ion batteries, primarily due to 1) its specific capacity of 4,200 $mAhg^{-1}$ and volume capacity of 9,786 mAh cm^{-3}, the highest known for a LIB anode; 2) relatively low working potential (0.5 V vs. Li/Li^+); and 3) the natural abundance of element Si and its environmental benignity.[8-10]

However, the practical implementation of Si anodes is still blocked due to three major problems. First, poor cycle-life of silicon materials results from pulverization during the huge volumetric fluctuations (>300 %) which accompany lithium ion intercalation and deintercalation. Second, drastic irreversible capacity loss and low coulombic efficiency is caused by mechanical fracture of Si anodes during the alloying/dealloying process. Finally, the solid electrolyte interphase (SEI) breaks as the nanostructure shrinks during delithiation. This results in the exposure of the fresh silicon surface to the electrolyte and the reformation of the SEI, resulting in the SEI growing thicker with each charge/discharge cycle, as shown in **Figure 1**.[11, 12]

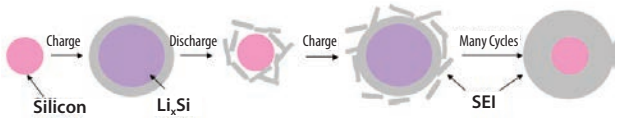

Figure1. Schematic of SEI formation on a pure silicon surface during charge/discharge cycles.

Nanostructured Silicon Anode Materials

To address these issues, several strategies have been developed to accommodate the huge volumetric changes. One effective strategy is to reduce the active particle size to the nanometer range, at which point, nanosized particles can accommodate significant stress without cracking, as well as decreasing the electronic and ionic transport distance. Moreover, the high density of grain boundaries in nanomaterials also provides a fast diffusion path for Li ions and acts as additional Li-storage sites.[13-16] Huang *et al.* have shown the effect of Si nanoparticle size on the release of structural stress by *in situ* transmission electron microscopy (TEM) and suggested the stored strain energy from electrochemical reactions was insufficient to drive crack propagation in Si nanoparticles if the particle diameter is <150 nm (**Figure 2**).[17] Recently, Kim et al. reported 5, 10, and 20 nm-sized Si nanoparticles can be synthesized under high pressure at 380 °C by using various surfactants.[18] Cycling these materials between 0 and 1.5 V at a rate of 0.2 C, a capacity of 2,500 mAh g^{-1} can be achieved for over 40 charge/discharge cycles with capacity retentions of 71, 81, and 67%, respectively.

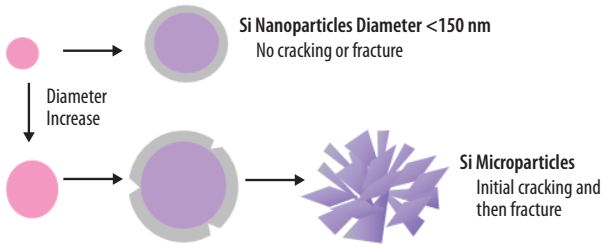

Figure 2. Schematic of the stability of silicon during cycles influenced by the diameter size.

Table1. Comparison of various anode materials.

Anode Materials	C	Li	Si	Sn	Sb	Al	Mg	$Li_4Ti_5O_{12}$	Bi
Lithiated phase	LiC_6	Li	$Li_{4.4}Si$	$Li_{4.4}Sn$	Li_3Sb	LiAl	Li_3Mg	$Li_{12}Ti_5O_{12}$	Li_3Bi
Theoretical specific capacity (mAh g_{-1})	372	3,862	4,200	994	660	993	3,350	175	385
Theoretical volume capacity (mAh cm^{-3})	837	2,047	9,786	7,246	4,422	2,681	4,355	613	3,765
Volume change (%)	12	100	320	260	200	96	100	1	215
Potential vs. Li (~v)	0.05	0	0.4	0.6	0.9	0.3	0.1	1.6	0.8

Kim *et al.* also reported an intriguing 3D bulk Si architecture with a highly interconnected porous structure.[19] With 40-nm thick pore-walls, this Si structure can accommodate large strains without pulverization, even after 100 cycles, and maintained a charge capacity of greater than 2,800 mA h g^{-1} at a rate of 1 C (2,000 mAg^{-1}). The Cui group at Stanford University reported silicon nanowire and nanotube anodes show high discharge capacities and stability over tens of cycles, with reversible capacities as high as ~3,200 $mAhg^{-1}$ (for nanowires) and ~3,247 $mAhg^{-1}$ (for nanotubes).[20,21] Nanowire- and nanotube-based electrodes can accommodate material expansion during cycling, as well as forming a direct current pathway when grown directly onto the current collector.[10] In addition, Si nanotubes increase the surface area accessible to the electrolyte, by allowing Li ions to intercalate at the interior and exterior of the nanotubes.

Despite the advantages of nanostructured Si anodes, nanosized particles also have disadvantages, such as large surface area, high manufacturing costs, and difficulty of handling.[22] Even so, nanostructured silicon is regarded as one of the most promising methods to overcome the challenges of silicon anodes for the next generation lithium-ion batteries.

Si-based Carbon Composite Anode Materials

Another approach to overcome the volume change during cycling is to form a composite material.[23] The matrix does not experience significant volumetric change, which may buffer the expansion of silicon, maintain the structural integrity of the electrode, and enhance stability by reducing silicon aggregation or electrochemical sintering.[10]

One promising research area is silicon-based carbon composites, the benefits of which are attributed to the improved electric conductivity and the expansion buffering effect of a carbon matrix.[24-27] In addition, the carbon additives have the advantages of exceptional ionic conductivity and Li- storage ability.[28,29] However, a conformal carbon coating on Si active material would rupture during cycling, resulting in Si exposure to electrolytes and additional SEI deposition. Therefore, a form of carbon coating that can accommodate the large volume fluctuation of Si is necessary.

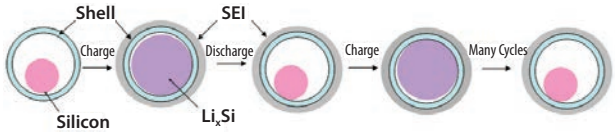

Figure 3. Schematic of yolk–shell structured Si hybrid in which the internal void space can accommodate Si volume expansion during lithiation, protecting the surface of the Si core from SEI deposition.

One effective approach is the introduction of abundant void space between Si and the carbon shell, as shown in **Figure 3**.[30] Liu *et al.* reported a yolk–shell structured Si@Carbon (**Figure 4A**) with excellent capacity (2,833 $mAhg^{-1}$ at C/10), cycle-life (1,000 cycles with 74% capacity retention), and coulumbic efficiency (99.84%).[31] Si nanoparticles were first coated with a SiO_2 layer and then with a polydopamine layer, which was subsequently carbonized to form a nitrogen-doped carbon coating, the yolk–shell Si@Void@C structure was obtained after selectively removing the SiO_2 layer by hydrofluoric acid (HF) treatment. Very recently, Li *et al.* reported hollow core shell porous Si–C nanocomposites with a reversible capacity of 650 mA h g^{-1} after 100 cycles (current density of 1 A g^{-1}), which corresponds to 86% capacity retention.[32] The advantage of these unique structures can be attributed to two aspects: 1) the void space between the Si core and the carbon shell allows for the Si nanoparticles to expand upon lithiation without breaking the shell; and 2) the electrical and ionic conductivities of a carbon shell improve the intercalation kinetics while preventing the electrolyte from reaching the Si surface.

Another strategy is to produce porous Si–C composites. Si–C porous composites with high capacity (reversible capacities: 1,950 mAh g^{-1}) and long cycling life were reported by Magasinski *et al.*[33] A hierarchical bottom-up assembly method was employed to fabricate the porous Si–C architecture in which irregular channels can ensure rapid access of Li ions into the particle bulk, while the particle's internal porosity can accommodate the large Si volume changes during cycling.

Graphene (Aldrich Prod. Nos. 773697, 773719, and 773700) has also been used in Si anodes to buffer the volume changes and improve electronic conductivities due to its superior electrical conductivity, high surface area (2,600 m^2 g^{-1}), excellent chemical stability, and strong mechanical strength.[34-38] Luo *et al.* reported crumpled capsules of graphene wrapped Si nanoparticles with high capacity (940 mAh g^{-1} after 250 cycles) and good cycling stability (capacity retention: 83%) synthesized by a one-step aerosol-assisted capillary assembly technique.[30] The folds and wrinkles in the crumpled graphene layer can accommodate the volume expansion of Si upon lithiation without fracture and protect Si nanoparticles from excessive deposition of the insulating SEI. More recently, Wen *et al.* reported the electrochemical performance of graphene-encapsulated Si anodes could be improved by treating the Si with aminopropyltrimethoxysilane (APS) (Aldrich Prod. No. 281778) and replacing carboxymethyl cellulose (CMC) with sodium alginate (Aldrich Prod. No. W201502), both of which could improve the interactions between the graphene-bonded and encapsulated Si groups and the current collector. These graphene-encapsulated functionalized Si nanoparticles exhibit a capacity of 2,250 mAh g^{-1} at 0.1 C and of 1,000 mAh g^{-1} at 10 C, and retain 85% of their initial capacity even after 120 cycles.

Si nanoparticles embedded in a 3D graphene scaffold (**Figure 4B**) were reported by Zhao et al., and exhibited a reversible capacity of approximately 3,200 mA g^{-1} (current density: 1 A g^{-1}), retaining 83% of its theoretical capacity after 150 cycles.[39] In this case, the 3D conducting graphenic scaffold was constructed with aligned graphene sheets derived from exfoliated graphene oxide by a facile wet chemical method. The ability to maintain a high capacity in this anode material was attributed to the excellent cross-plane ion diffusivity which shortens Li diffusion paths throughout the electrode, allowing full access to the interior and rapid lithiation and delithiation reactions in the Si nanoparticles. Xin et al. also reported the synthesis of a Si/graphene nanocomposite with a 3D porous architecture through a series of chemical processes.[40] This architecture delivers a reversible capacity of 900 mAh g^{-1} with very little fading after 30 cycles even at charge rates of 1 A g^{-1}. The 3D graphene-based composite displays superior cycling stability and high rate performance due to enhancement of the electrical conductivity of the electrode by the 3D graphene network, demonstrating superior rate characteristics over the 2D nanostructure.

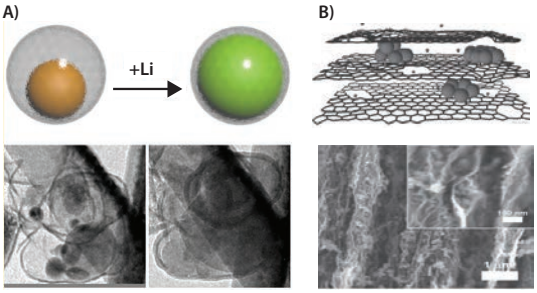

Figure 4. **A)** A schematic drawing of an individual Si@Void@C particle (top) and *in situ* TEM images of synthesized Si@Void@C powder before and after lithiation and delithiation (below). Reproduced with permission from Reference 31. Copyright 2012 American Chemical Society. **B)** A schematic drawing (top) of a section of a composite electrode material constructed with a graphenic scaffold with in-plane carbon vacancy defects. (Si: large particles; Li ions: small spheres) and SEM image (below) of the cross-section of a Si–3D graphenic scaffold, the inset shows Si nanoparticles embedded between graphene sheets uniformly. Adapted from Reference 39. Copyright 2011 Wiley-VCH.

Future Directions

Very recently, Wu *et al.* reported ideal 3D porous Si/conductive polymer hydrogel composite electrodes with relatively stable reversible capacity (1,600 mAh g^{-1} after 1,000 deep cycles) and very stable performance (cycled 5,000 times without significant capacity decay).[2] The porous hierarchical hydrogel framework has significant advantages: the conductive polymer 3D network provides fast electronic and ionic transfer channels, in addition to porous space for volume expansion of Si particles. This fabrication method of *in situ* polymerization shows scalability and promise for industrial commercialization, as shown in **Figure 5**.

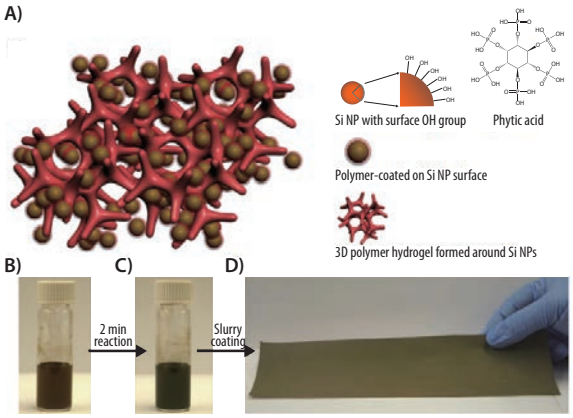

Figure 5. Schematic illustration of 3D porous Si nanoparticles/conductive polymer hydrogel composite electrodes (**A**), in which each Si nanoparticle is encapsulated within a conductive polymer surface coating and is further connected to the highly porous hydrogel framework, and photographs (**B–D**) showing the key steps of the electrode fabrication process. Adapted from Reference 2. Copyright 2013 Nature Publishing Group.

Summary and Challenges

Silicon is one of the most promising anode materials for lithium-ion batteries due to advantages including its highest known capacity and relatively low working potential. However, the problem of extremely large volumetric change must be overcome before silicon anodes can be utilized in practical lithium batteries. In this micro-review, various silicon anodes and silicon-based composite anodes with improved electrochemical performance have been elucidated, showing two viable solutions to circumvent the Si anode. Further research is still needed to address the practical requirements for Si anodes, including high power density, long life, simple manufacturing, and low cost.

Acknowledgments

The authors greatly acknowledge the financial support by the Shanghai Municipal Natural Science Foundation (12ZR1414300), the National Natural Science Foundation of China (51172142, 51302169), the Starting Foundation for New Teacher of Shanghai Jiao Tong University (12X100040119), the Scientific Research Foundation for Returned Overseas Chinese Scholars, State Education Ministry, and the Third Phase of 211 Project for Advanced Materials Science (WS3116205007).

References

(1) "Lithium-Ion Battery Market Set for Boom Courtesy of Hybrid and Electric Vehicles" IHS Isuppli Market Research. http://www.isuppli.com/semiconductor-value-chain/news/pages/lithium-ion-battery-market-set-for-boom-courtesy-of-hybrid-and-electric-vehicles.aspx
(2) Wu, H.; Yu, G.; Pan, L.; Liu, N.; McDowell, M. T.; Bao, Z.; Cui, Y., *Nature Communications* **2013**,*4*, doi: 10.1038/ncomms2941.
(3) Song, X. F., *Nanotechnology*, **2013**, *24*, 205401.
(4) Tang, K.; White, R. J.; Mu, X.; Titirici, M. M.; van Aken, P. A.; Maier, J., *ChemSusChem*, **2012**, *5*, 400.
(5) Yi, T. F.; Jiang, L. J.; Shu, J.; Yue, C. B.; Zhu, R. S.; Qiao, H.-B., *Journal of Physics and Chemistry of Solids*, **2010**, *71*, 1236.
(6) A. Trifonova; M. Wachtler; Winter, M., Besenhard, J. O., *Ionics*, **2002**, *8*, 321.
(7) Yan, J. M.; Huang, H. Z.; Zhang, J.; Liu, Z. J.; Yang, Y., *Journal of Power Sources*, **2005**, *146*, 264.
(8) Zhang, W. J., *Journal of Power Sources*, **2011**, *196*, 13.
(9) Wu, H.; Zheng, G.; Liu, N.; Carney, T. J.; Yang, Y.; Cui, Y., *Nano Letters*, **2012**, *12*, 904.
(10) Szczech, J. R.; Jin, S., *Energy & Environmental Science*, **2011**, *4*, 56.
(11) Wu, H.; Cui, Y., *Nano Today*, **2012**, *7*, 414.
(12) Wu, H.; Chan, G.; Choi, J. W.; Ryu, I; Yao, Y.; McDowell, M. T.; Lee, S. W.; Jackson, A.; Yang, Y.; Hu, L. B.; Cui, Y., *Nature Nanotechnology*, **2012**, *7*, 310.
(13) Kim, I. S; Blomgren, G. E.; Kumta, P. N., *Electrochemical and Solid-State Letters*, **2003**, *6*, A157.
(14) Beaulieu, L. Y.; Larcher, D.; Dunlap, R. A.; Dahn, J. R., *Journal of The Electrochemical Society*, **2000**, *147*, 3206.
(15) Todd, A. D. W.; Ferguson, P. P.; Barker, J. G.; Fleischauer, M. D.; Dahn, J. R., *Journal of The Electrochemical Society*, **2009**, *156*, A1034.
(16) Yang, J.; Winter, M.; Besenhard, J. O., *Solid State Ionics*, **1996**, *90*, 281.
(17) Liu, X. H.; Zhong, L.; Huang, S.; Mao, S. X.; Zhu, T.; Huang, J. Y., *ACS NANO*, **2012**, *6*, 1522.
(18) Kim, H.; Seo, M.; Park, M. H.; Cho, J., *Angewandte Chemie International Edition*, **2010**, *49*, 2146.
(19) Kim, H.; Han, B.; Choo, J.; Cho, J., *Angewandte Chemie International Edition*, **2008**, *47*, 10151.
(20) Chan, C. K.; Peng, H.; Liu, G.; McIlwrath, K.; Zhang, X. F.; Huggins, R. A.; Cui, Y., *Nature Nanotechnology*, **2007**, *3*, 31.
(21) Park, M. H.; Kim, M. G.; Joo, J.; Kim, K.; Kim, J.; Ahn, S.; Cui, Y.; Cho, J., *Nano Letters*, **2009**, *9*, 3844.
(22) Arico, A. S.; Bruce, P.; Scrosati, B.; Tarascon, J. M.; Schalkwijk, W. V., *Review Article*, **2005**, *4*, 366.
(23) Liu, H. K.; Guo, Z. P.; Wang, J. Z.; Konstantinov, K., *Journal of Materials Chemistry*, **2010**, *20*, 10055.
(24) Dimov, N.; Kugino, S.; Yoshio, M., *Electrochimica Acta*, **2003**, *48*, 1579.
(25) Yoshio, M.; Wang, H.; Fukuda, K.; Umeno, T.; Dimov, N.; Ogumi, Z., *Journal of The Electrochemical Society*, **2002**, *149*, A1598.
(26) Chen, P. C.; Xu, J.; Chen, H.; Zhou, C., *Nano Research*, **2010**, *4*, 290.
(27) Li, H.; Huang, X. J.; Chen, L. Q.; Wu, Z. G.; Liang, Y., *Electrochemical and Solid-State Letters*, **1999**, *2*, 547.
(28) Lee, H. Y.; Lee, S. M., *Electrochemistry Communications*, **2004**, *6*, 465.
(29) Saint, J.; Morcrette, M.; Larcher, D.; Laffont, L.; Beattie, S.; Pérès, J. P.; Talaga, D.; Couzi, M.; Tarascon, J. M., *Advanced Functional Materials*, **2007**, *17*, 1765.
(30) Luo, J.; Zhao, X.; Wu, J.; Jang, H. D.; Kung, H. H.; Huang, J., *The Journal of Physical Chemistry Letters*, **2012**, *3*, 1824.
(31) Liu, N.; Wu, H.; McDowell, M. T.; Yao, Y.; Wang, C.; Cui, Y., *Nano Letters*, **2012**, *12*, 3315.
(32) Li, X.; Meduri, P.; Chen, X.; Qi, W.; Engelhard, M. H.; Xu, W.; Ding, F.; Xiao, J.; Wang, W.; Wang, C.; Zhang, J. G.; Liu, J., *Journal of Materials Chemistry*, **2012**, *22*, 11014.
(33) Magasinki, A.; Dixon, P.; B. Hertzberg; A. Kvit; J. Ayala; Yushin, G., *Nature materials*, **2010**, *9*, 353.
(34) Lee, J. K.; Smith, K. B.; Hayner, C. M.; Kung, H. H., *Chemical Communications*, **2010**, *46*, 2025.
(35) Tao, H. C.; Fan, L. Z.; Mei, Y.; Qu, X., *Electrochemistry Communications*, **2011**, *13*, 1332.
(36) Chou, S. L.; Wang, J. Z.; Choucair, M.; Liu, H. K.; Stride, J. A.; Dou, S. X., *Electrochemistry Communications*, **2010**, *12*, 303.
(37) Stankovich, S.; Dikin, D. A.; Dommett, G. H. B.; Kohlhaas, K. M.; Zimney, E. J.; Stach, E. A.; Piner, R. D.; Nguyen, S. T.; Ruoff, R. S., *Nature*, **2006**, *442*, 282.
(38) Wen, Y.; Zhu, Y.; Langrock, A.; Manivannan, A.; Ehrman, S. H.; Wang, C., *Small*, **2013**, doi: *10*.1002.
(39) Zhao, X.; Hayner, C. M.; Kung, M. C.; Kung, H. H., *Advanced Energy Materials*, **2011**, *1*, 1079.
(40) Xin, X.; Zhou, X.; Wang, F.; Yao, X.; Xu, X.; Zhu, Y.; Liu, Z., *Journal of Materials Chemistry*, **2012**, *22*, 7724.

Lithium-Ion Battery Anode Materials

For a complete list of lithium-ion battery anode materials, visit aldrich.com/lib.

Product Name	Composition	Dimensions	Purity	Form	Prod. No.
Lithium titanate, spinel, LTO nanopowder	$Li_4Ti_5O_{12}$	particle size <200 nm (BET)	>99%	nanopowder	702277-25G
Lithium titanate, LTO	Li_2TiO_3	–325 mesh	-	powder	400939-100G
Lithium-aluminum alloy	Al-Li	-	-	powder	426490-25G
Tin(IV) oxide	SnO_2	particle size <100 nm (BET)	-	nanopowder	549657-5G 549657-25G
Lithium	Li	particle size 4-10 mesh	99%, metals basis	granular	444456-10G 444456-50G
	Li	thickness × W 1.5 × 100 mm	99.9% trace metals basis	ribbon	266000-25G 266000-100G
	Li	thickness × W 0.75 × 45 mm	99.9% trace metals basis	ribbon	265993-25G 265993-100G
	Li	thickness × W 0.38 × 23 mm	99.9% trace metals basis	ribbon	265985-25G 265985-100G
	Li	diam. 3.2 mm	≥98%	wire	278327-25G 278327-100G
Graphite	C	O.D. × I.D. × L 200-500 nm × 1-10 nm × 10-40 µm particle size 200-500 nm	95% trace metals basis	powder	636398-2G 636398-10G
	C	<45 µm	≥99.99%	powder	496596-113.4G
	C	D × L 50-250 nm × 0.5-5 µm 100 nm (average width, TEM) 2.5 µm (average length, TEM)	98% carbon basis	powder	698830-1G
Carbon, mesoporous	C	particle size <500 nm (DLS)	>99.95% trace metals basis	nanopowder	699624-5G 699624-25G
Carbon	C	2 - 12 µm	99.95% trace metals basis	glassy, spherical powder	484164-10G 484164-50G

Silicon Pieces and Silicon Nanomaterials

For a complete list of silicon pieces and silicon nanomaterials, visit aldrich.com/periodic.

Product Name	Description	Purity	Form	Prod. No.
Silicon	-	99.95% trace metals basis	pieces	343250-50G 343250-500G
	–60 mesh	99.999% trace metals basis	powder	267414-25G
	–325 mesh	99% trace metals basis	powder	215619-50G 215619-250G 215619-1KG
	particle size <100 nm (TEM)	≥98% trace metals basis	nanopowder	633097-10G 633097-25G

Silicon Dioxide: Porous and Nanostructured Materials

For a complete list of silicon dioxide: porous and nanostructured materials, visit aldrich.com/periodic.

Product Name	Particle Size and Pore Dimensions	Form	Prod. No.
Silica	primary particle size 12 nm (TEM)	nanopowder	718483-100G
	particle size 200 nm pore size 4 nm	mesoporous nanoparticles	748161-5G
Silica, mesostructured	pore volume 2.31 cm^3/g	powder	560979-10G
	pore size 2-4 nm pore volume 1-2 cm^3/g	powder	541036-5G 541036-25G
	pore size ~ 7.1 nm pore volume 0.91 cm^3/g	powder	643637-5G 643637-25G
	pore size 2.1-2.7 nm pore volume 0.98 cm^3/g	powder	643645-5G 643645-25G
Silicon dioxide	particle size 10 - 20 nm (BET)	nanopowder	637238-50G 637238-250G 637238-500G
	particle size 5 - 15 nm (TEM)	nanopowder (spherical, porous)	637246-50G 637246-250G 637246-500G
Silicon dioxide, alumina doped	particle size <50 nm	dispersion nanoparticles	701491-25ML 701491-100ML

Graphene and Graphene Oxide

For a complete list of graphene and graphene oxide, visit aldrich.com/graphene.

Structure	Product Name	Description	Properties	Prod. No.
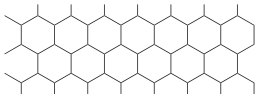	Monolayer graphene film, 1 cm x 1 cm on copper foil	L × W × thickness 1.5 cm × 1.5 cm × 25 µm (Copper foil substrate) L × W × thickness 1 cm × 1 cm × (theoretical) 0.345 nm (Monolayer graphene film)	resistance 600 Ω/sq	773697-4EA
	Monolayer graphene film, 1 cm x 1 cm on quartz	L × W × thickness 1 cm × 1 cm × (theoretical) 0.345 nm (Monolayer graphene film) L × W 1.25 × 1.25 cm (Quartz)	resistance 600 Ω/sq	773719-4EA
	Monolayer graphene film, 1 cm x 1 cm on SiO_2/Si substrate	L × W × thickness 1.25 cm × 1.25 cm × 525 µm (SiO_2/Si substrate) L × W × thickness 1 cm × 1 cm × (theoretical) 0.345 nm (Monolayer graphene film)	resistance 600 Ω/sq	773700-4EA
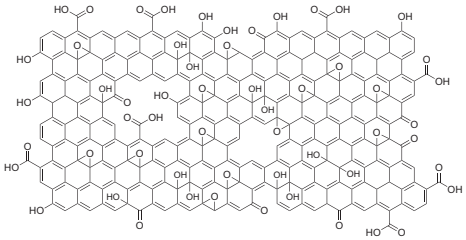	Graphene oxide	2 mg/mL	dispersion in H_2O	763705-25ML 763705-100ML
	Graphene oxide	4 mg/mL	dispersion in H_2O	777676-50ML 777676-200ML
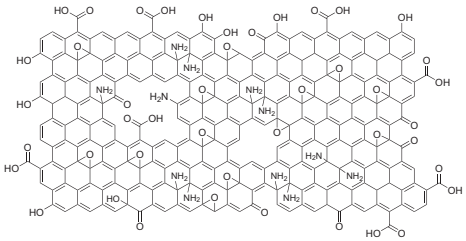	Graphene oxide, ammonia functionalized	-	flakes	777013-250MG

Precursors for Fabrication of Silicon Nanomaterials

For a complete list of precursors for fabrication of silicon nanomaterials, visit aldrich.com/mnel.

Product Name	Composition	Purity	Form	Prod. No.
(3-Aminopropyl)triethoxysilane	$H_2N(CH_2)_3Si(OC_2H_5)_3$	≥98.0%	liquid	741442-100ML 741442-500ML
Hexamethyldisilane	$(Si(CH_3)_3)_2$	98%	liquid	217069-5G 217069-10G 217069-50G
Tetraethyl orthosilicate	$Si(OC_2H_5)_4$	99.999% trace metals basis	liquid	333859-25ML 333859-100ML
Tetramethylammonium silicate solution	$(CH_3)_4N(OH) \cdot 2SiO_2$	≥99.99% trace metals basis	liquid	438669-100ML 438669-500ML
Tetramethyl orthosilicate	$Si(OCH_3)_4$	≥98% ≥99.9% trace metals basis, deposition grade	liquid	679259-50G

Atomic Layer Deposition of Nanomaterials for Li-Ion Batteries, Fuel Cells, and Solar Cells

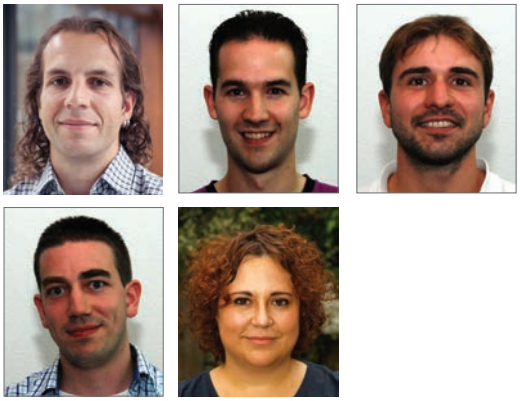

Erwin Kessels,* Harm Knoops, Matthieu Weber,
Adrie Mackus, and Mariadriana Creatore
Department of Applied Physics, Eindhoven University of Technology
P.O. Box 513, 5600 MB Eindhoven, The Netherlands
*Email: w.m.m.kessels@tue.nl

Introduction

Nanomaterials are considered a route to the innovations required for large-scale implementation of renewable energy technologies in society to make our life sustainable. This holds both for energy harvesting and for energy storage devices. In recent years, this has spurred many research activities on 0D (nanoparticles), 1D (nanowires and nanotubes), and 2D (such as graphene) materials—which can serve as elemental building blocks of device elements—while there also has been a lot of emphasis on 3D nanostructuring in general. Many challenges arise when building devices from nanomaterials, particularly in the preparation of these nanomaterials as well as in their modification, functionalization, and stabilization.

Vapor phase deposition processes are one class of methods that can be used to address these challenges. For example, nanoparticles, nanowires, nanotubes, and graphene can all be grown from the vapor phase. This also holds for thin films that can be used to modify, functionalize, and stabilize the nanomaterials or to build nanostructured materials. One vapor phase deposition technique that is receiving growing attention is atomic layer deposition (ALD). The application of this technique for building energy harvesting and energy storage devices will be addressed in this article. In the next sections, the preparation of thin films and nanoparticles by ALD will be addressed and recent progress in the application of ALD-prepared nanomaterials in Li-ion batteries, fuel cells, and solar cells will be briefly reviewed on the basis of selected examples.

Atomic Layer Deposition of Thin Films and Nanoparticles

ALD is a cyclic vapor phase deposition technique in which precursors and reactants are injected into the reactor chamber alternately (see **Figure 1A**) and in which the reactions are driven by the surface chemistry and not by thermal decomposition.[1] A prerequisite for ALD is that the surface chemistry in the half-reactions of the ALD cycles is self-limiting. This allows for a precise growth control with Ångstrom-level resolution as well as an excellent uniformity and conformality on demanding substrate topologies. In addition, ALD affords the deposition of high-quality materials at rather low substrate temperatures. Typical substrate temperatures range from 400 °C down to room temperature, depending on the material and the process. Moreover, ALD is a scalable technology that has already been implemented in the manufacturing of hard-disk read heads, memory, and logic devices.

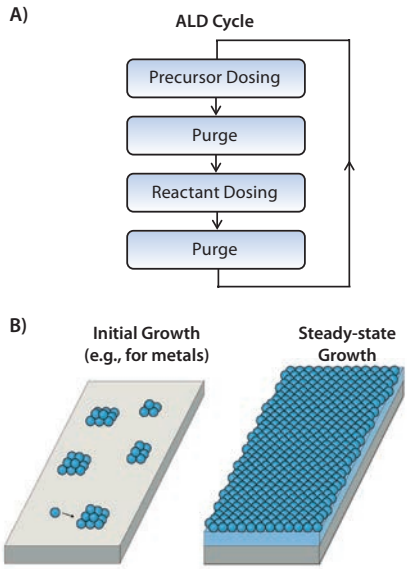

Figure 1. A) Schematic representation of an ALD cycle consisting of two half-cycles in which precursor and reactant dosing are alternated and separated by purge steps. **B)** Initial and steady-state growth conditions during ALD leading to nanoparticles (e.g., for metal ALD processes) and closed, conformal films, respectively.

ALD leads to layer-by-layer growth of amorphous or polycrystalline thin films (see **Figure 1B**) under regular circumstances. Such a layer is deposited every cycle and corresponds to less than a monolayer of material as typical "growth-per-cycle" values range from 0.25 to 1.5 Å. However, during initial growth the process can deviate significantly from the steady-state growth conditions. Growth can be inhibited or in some cases even enhanced depending on the substrate, its pretreatment, and the material deposited.[2] For example, for metals deposited on oxide or oxidized substrates, it has clearly been established that initial growth takes place in the

Volmer-Weber mode instead of layer-by-layer mode. This means that, initially, islands of metal atoms are formed (see **Figure 1B**) which grow in size every ALD cycle due to sticking of atoms directly from the gas phase or indirectly by surface diffusion processes.[3] After a certain number of cycles, the islands start to coalesce and a closed film is obtained. This implies that metal nanoparticles can also be deposited via ALD by exploiting the island growth in the initial ALD cycles. The ALD cycles need to be halted before coalescence occurs and the size of the nanoparticles can be accurately controlled by carefully selecting the number of cycles. **Figure 2** illustrates the opportunities provided by ALD in terms of depositing nanoparticles and conformal films, both on planar substrates as well as on carbon nanotubes, nanowires, and 3D-structured substrates.

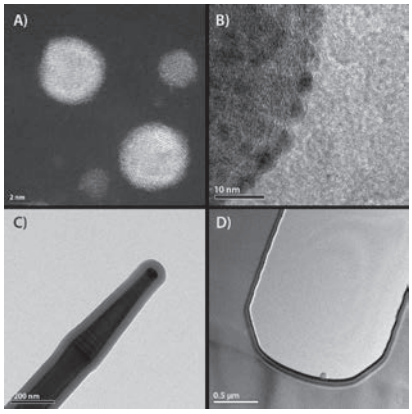

Figure 2. Examples of nanoparticles and films deposited by ALD on various substrate materials. **A)** Core/shell nanoparticles of Pd/Pt on a planar oxide substrate. **B)** Pd nanoparticles on a multiwall carbon nanotube. **C)** GaP nanowire covered by thin film of Al_2O_3. **D)** Trench in silicon covered by a stack of Al_2O_3/TiN/Al_2O_3/TiN. The scale bars in **A)–D)** are 2 nm, 10 nm, 200 nm, and 0.5 µm, respectively.

Li-Ion Batteries, Fuel Cells, and Solar Cells

Lithium-Ion Batteries

Li-ion batteries are currently considered as energy storage solution for a wide range of applications, from electrical vehicles to microsystems. To reach improvements in terms of capacity, power, and lifetime, there is a trend toward nanostructuring of the electrode materials while there are also several other efforts to vigorously change the battery configuration.[4] The latter includes, for example, all-solid-state Li-ion batteries built from thin films, where 3D structuring is also proposed. ALD is considered an enabling technology for several concepts of nanostructured Li-ion batteries.[5]

In **Figure 3**, the potential of ALD is schematically illustrated for three battery concepts; i.e., particle-based electrodes, 3D-structured electrodes, and 3D all-solid-state microbatteries. Electrodes in commercial batteries are most often based on micrometer-sized particles of active materials, which are mixed with binder compounds and conductive additives. **Figure 3A** illustrates a particle-based cathode. The liquid electrolyte penetrates the porous network, facilitating the Li^+ transport. When going to smaller particle sizes to increase the surface-to-volume ratio and hence the power capablity, the decomposition of the electrolyte by the so-called solid electrolyte interphase (SEI) formation can also be increased. This adverse effect can be reduced or possibly prevented by modifying the surface of the particles by applying a passivating or protective film. Such films need to be ultrathin to have high Li^+ and electron conductivities while excellent conformality is needed to be sufficiently protective. Researchers from the University of Colorado at Boulder and the National Renewable Energy Laboratory (NREL) have successfully pioneered the protection of particles by ALD-prepared films. For example, improved stability was demonstrated by depositing Al_2O_3 (Aldrich Prod. Nos. 718475 and 634875) on $LiCoO_2$ (Aldrich Prod. No. 442704) particles.[6] It was also shown Al_2O_3 improves the cycle-life of natural graphite anodes.[7] In the latter case, it was found the best cycle-life was not obtained by directly coating the individual particles but by first composing the electrode and carrying out the ALD cycles with $Al(CH_3)_3$ (Aldrich Prod. No. 663301) and H_2O dosing afterward. Furthermore, the improvement in stability was obtained for extremely thin layers (i.e., only a few ALD cycles) which might indicate the positive effect may not require a closed Al_2O_3 film.[7]

ALD has also been used in 3D-structured electrodes, in which the electrode is specifically designed such that diffusion paths in the materials are short, which improved transport of electrons and Li^+. **Figure 3B** shows an example of such a structure. Nanowires of Al serve as current collectors and allow for easy transport of electrons to the active material deposited on the nanowires. Moreover, Li^+ transport is facilitated by the open structure in which the electrolyte can penetrate easily. This design was taken by Cheah *et al.* who coated the Al nanowires with TiO_2 using ALD.[8] The TiO_2 was used as the anode electrode material. TiO_2 has a relatively high redox potential, alleviating problems with electrolyte decomposition. Similarly, Kim *et al.* created a hollow TiO_2 nanonetwork by depositing a thin film of TiO_2 on a peptide assembly. This assembly was subsequently removed by a high temperature step which also resulted in crystallization of the TiO_2 film into the anatase phase.[9] In both cases, a high capacity and high rate capability were observed.

There is a growing interest in Li-ion microbatteries for which the challenge is to achieve a high energy density at small device dimensions.[4] The designs for such microbatteries are typically all-solid-state as packaging methods do not scale very well. Moreover, for all-solid-state batteries, electrolyte decomposition issues are greatly reduced, which extends the cycle-life. The batteries consist of thin films with limited thickness due to the low Li^+ and electron diffusion in solid materials. 3D structuring is considered necessary to increase the storage capacity without deteriorating the power capacity. Notten *et al.* proposed a system-in-package solution consisting of a 3D topology etched into Si substrates in which the battery stack is deposited[10] (see **Figure 3C**). In this stack, the electrolyte separates the electrodes, which in turn are both connected to the electrical circuit by current collectors. Furthermore, the battery stack needs to be encapsulated from the environment and a Li-diffusion barrier is necessary to avoid loss of Li into the Si substrate. Since all layers need to be deposited as thin films in the 3D topology, ALD or very conformal CVD processes are required to build such a battery stack. The first stage of the research on this kind of microbatteries focused on the deposition of passive battery materials. It was, for example, demonstrated that TiN (Aldrich Prod. No. 595063) deposited by ALD from $TiCl_4$ (Aldrich Prod. No. 697079) and H_2-N_2 plasma was well-suited as a Li-diffusion barrier and current collector even though the TiN was not fully conformal.[11] Furthermore, current collectors of Pt were prepared successfully by ALD from $MeCpPtMe_3$ (Aldrich Prod. No. 697540) and O_2 gas, although it was found the Pt needed special surface preparation to achieve a good adhesion.[5]

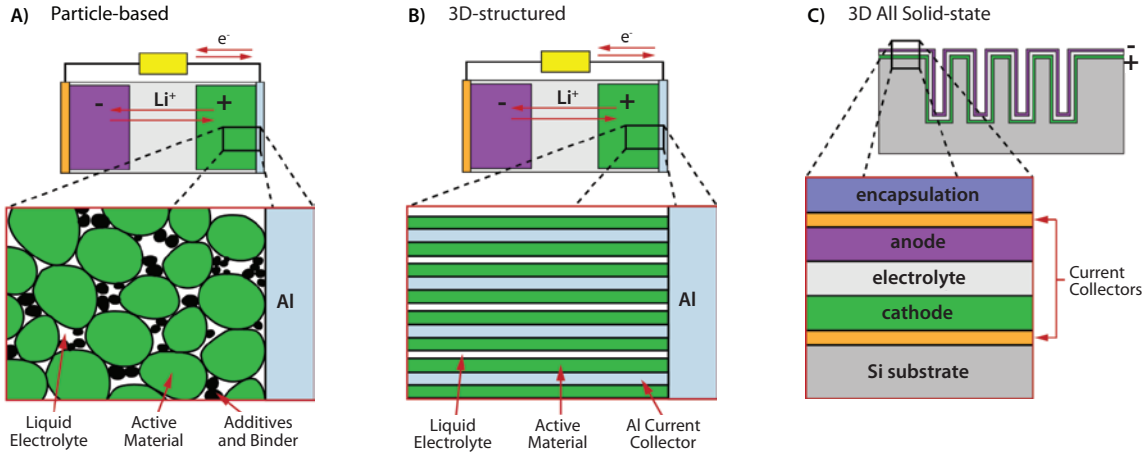

Figure 3. Various configurations of Li-ion batteries involving ALD-prepared films. Li-ion battery with **A)** particle-based electrode in which the particles are covered by an ultrathin ALD film for protection/stabilization against the liquid electrolyte and **B)** a nanostructured electrode to reduce Li and electron diffusion paths, to absorb volume changes to avoid cracking and crumbling of the material, and to increase storage capacity due to nanosize effects. In **A)** and **B)**, the liquid electrolyte is able to penetrate into the porous electrode structures. **C)** An all-solid-state Li-ion battery consisting of a stack of active and passive thin film battery materials. A 3D-structured substrate is used to increase the storage capacity per unit of surface area and this requires conformal deposition techniques such as ALD.

In the second stage of the research, active battery materials were considered. For example, electrochemical testing revealed Co_3O_4 (Aldrich Prod. Nos. 637025, 203114, and 221643) deposited by ALD from $CoCp_2$ (Aldrich Prod. No. 339164) and O_2 plasma is a good thin film anode material.[12] In follow-up work, it was demonstrated ALD-prepared $LiCoO_2$ was electrochemically active as an anode material.[13] This material was deposited by combining Co_3O_4 and Li_2CO_3 (Aldrich Prod. No. 752843) deposition (from LiO *t*-Bu and O_2 plasma) in so-called supercycles, and electrochemical activity was achieved after crystallization of the material by high-temperature annealing. In recent years, several more Li-based materials have been deposited by ALD processes, although experiments in which the materials are electrochemically active are still relatively rare. This holds for both the Li-containing cathode and electrolyte materials as well as for the anode materials. Another challenge is the deposition of these materials in 3D topologies as well as the demonstration of functional microbattery devices.

Fuel Cells and Solar Cells

Similar nanostructuring approaches as the ones for Li-ion batteries are being considered for other energy technology devices such as fuel cells and solar cells. Research on solid oxide fuel cells (SOFCs), containing a solid metal oxide as electrolyte, concentrates on reducing the operating temperature from traditional values near 1,000 °C to lower temperatures of 500–800 °C. These high temperatures are required for conduction of oxygen ions through the metal oxide which acts as a membrane. One approach is the reduction of the resistance of the electrolyte by decreasing its thickness. To investigate electrolytes at nanometer scale thickness, several groups deposited yttria-stabilized zirconia (YSZ) (Aldrich Prod. Nos. 734683 and 774049) by ALD supercycles of Y_2O_3 (Aldrich Prod. Nos. 774022 and 544892) and ZrO_2 (Aldrich Prod. Nos. 774030 and 544760).[14] With respect to solar cells, many applications of ALD-prepared thin films have been considered in accordance with the variety in solar cell devices.[15,16] Excellent passivation of the surfaces of crystalline silicon solar cells has been achieved by ALD Al_2O_3 films. This has even lead to industrial ALD reactors based on the spatial ALD method in order to reach the high throughput required.[17] Copper indium gallium (di) selenide (CIGS) solar cells can benefit from the application of ALD buffer layers which are Cd-free. Zinc oxide compounds, such as (Zn,Mg)O and Zn(O,S), as well as films of In_2S_3 (Aldrich Prod. No. 308293) have mainly been considered for this purpose.[18] In dye-sensitized solar cells ALD films have been applied as a compact layer to prevent the backward electron transfer from TCO to the electrolyte.[19] Furthermore, much research has been carried out on barrier layers for various photoanode structures. For instance, TiO_2 nanoparticles (Aldrich Prod. Nos. 700347, 700355, and 700339) coated uniformally with thin passivating Al_2O_3 films resulted in improved solar cell performances which are related to the high recombination energy barrier of the Al_2O_3-TiO_2 interface, the high work function of the Al_2O_3 barrier, and the low energy barrier between the dye and Al_2O_3.[19,20] Furthermore, ALD films are also excellent moisture permeation barriers that have been successfully used to encapsulate flexible CIGS and organic solar cells.[21]

All aforementioned examples of applications of ALD in fuel cells and solar cells concerned thin films. There are, however, some cases in which nanoparticles synthesized by ALD can be used in such devices. For example, fuel cells require catalyst layers for reduction and oxidation reactions at the electrode/electrolyte interface. ALD Pt can be used for these applications, not only as ultrathin films[22] but also as nanoparticles. An example of a direct methanol fuel cell (DMFC) with nanoparticles as a catalyst is shown in **Figure 4A**. In such a DMFC, methanol is oxidized and O_2 is reduced on catalyst particles leading to CO_2 and H_2O. These catalyst particles can be mono- or bimetallic nanoparticles of Pt and/or

Ru. The nanoparticles are typically supported on carbon black but, alternatively, a carbon nanotube network structure can be used. Nanoparticles can be deposited on and into this carbon nanotube network structure by ALD.[23] Similarly, in dye-sensitized solar cells Pt nanoparticles (Aldrich Prod. No. 773875) prepared by ALD can be used. Pt is typically applied on the counter electrode (e.g., a transparent conductive oxide) by sputtering or electrodeposition and it catalyzes the electrolyte reduction process from I_3^- to $3I^-$ through the electrons arriving from the external circuit. However, for flexible dye-sensitized solar cells a transparent counter electrode is required to enable back-side illumination because preparation of the nanocrystalline TiO_2 photoanode is incompatible with the temperature-sensitive transparent polymer foils. This implies the Pt layer at the counter electrode needs to have both a high catalytic activity and a high transparency. This can only be reached by employing a low, yet efficient loading of well-dispersed nanoparticles. These can be deposited by ALD, albeit with an adapted process to enable low temperature processing.[24]

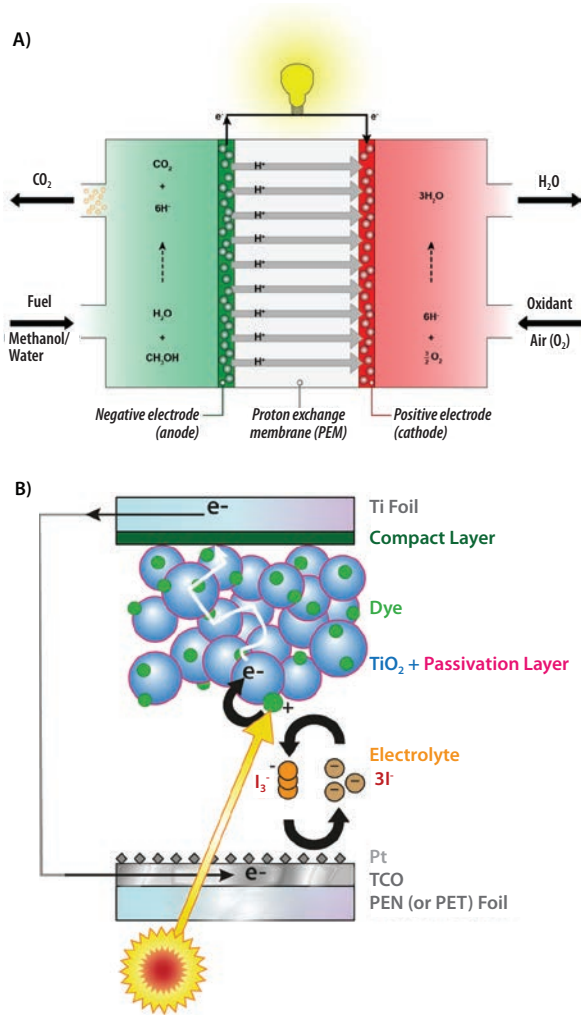

Figure 4. Applications that can benefit from the deposition of noble metal nanoparticles by ALD. **A)** Direct methanol fuel cell with electrodes containing noble metal nanoparticles. The nanoparticles can be deposited on and into the electrode material by ALD. **B)** A flexible dye-sensitized solar cell built up from polymer and metal foils. Light is entering from the "back side" of the cell through the counter electrode. A high transparency can be obtained by a counter electrode consisting of a transparent conductive oxide decorated with ALD Pt nanoparticles.

Summary

Selected examples of the recent progress in the application of ALD to Li-ion batteries, fuel cells, and solar cells have been addressed here. This progress clearly demonstrates ALD is an enabling technology to synthesize, modify, functionalize, or stabilize high-performance nanomaterials used in energy harvesting and storage devices. It also highlighted that ALD cannot only be used to deposit thin films, but it is also a promising technique for the synthesis of metal nanoparticles. Furthermore, it is noted ALD is a scalable method. Scalable methods are a prerequisite for manufacturing when aiming at the wide-scale implementation of energy technologies in our society. However, ALD has yet to provide a track record in low-cost, high-throughput processing. This means that other methods might be preferable to ALD when such alternative methods become available. In such cases, ALD can still be of key importance as it can serve as a method to demonstrate technological feasibility of devices and provide an excellent starting point for model studies.

Acknowledgment

Prof. Peter Notten of the Eindhoven University of Technology (TU/e), Dr. Leif Christensen of the Danish Technological Institute (DTI), and Dr. Thomas Brown of the University of Rome–Tor Vergata and their co-workers are acknowledged for the scientific discussions and collaborations. The members of the Plasma & Materials Processing group (TU/e) are thanked for their contributions to the research and a special thank you goes out to Dr. Marcel Verheijen (TU/e) for the electron microscopy images.

References

(1) George, S.M., *Chem. Rev.,* **2010**, *110*, 111.
(2) Puurunen, R.L., *J. Appl. Phys.,* **2005**, *97*, 121301.
(3) Mackus, A.J.M., Verheijen, M.A., Leick, N., Bol, A.A., Kessels, W.M.M., *Chem. Mater.* **2013**, *25*, 1905.
(4) Armand, M., Tarascon, J.M., *Nature,* **2008**, *451*, 652.
(5) Knoops, H.C.M., Donders, M.E., van de Sanden, M.C.M., Notten, P.H.L., Kessels, W.M.M., *J. Vac. Sci. Technol. A*, **2012**, *30*, 010801-1.
(6) Scott, I.D., Jung, Y.S., Cavanagh, A.S., Yan, Y., Dillon, A.C., George, S.M., Lee, S.H., *Nano Lett.* **2011,** *11*, 414.
(7) Jung, Y.S., Cavanagh, A.S., Riley, L.A., Kang, S.-H., Dillon, A.C., Groner, M.D., George, S.M., Lee, S.-H., *Adv. Mater.* **2010**, *22*, 2172.
(8) Cheah, S.K., Perre, E., Rooth, M., Fondell, M., Hårsta, A, Nyholm, L., Boman, M., Gustafsson, T., Lu, J., Simon, P., Edström, K., *Nano Letters* **2009**, *9*, 3230.
(9) Kim, S.W., Han, T.H., Kim, J., Gwon, H., Moon, H.S., Kang, S.W., Kim, S.O., Kang, K., *ACS Nano* **2009**, *3*, 1085.
(10) Notten, P.H.L., Roozeboom, F., Niessen, R.A.H., and Baggetto, L., *Adv. Mater.* **2007**, *19*, 4564.
(11) Baggetto, L., Knoops, H. C. M., Niessen, R.A.H., Kessels, W.M.M., Notten, P.H.L., *J. Mater. Chem.* **2010**, *20*, 3703.
(12) Donders, M.E., Knoops, H.C.M., Kessels, W.M.M., Notten, P.H.L., *J. Power Sources* **2012**, *203*, 72.
(13) Donders, M.E., Arnoldbik, W.M., Knoops, H.C.M., Kessels, W.M.M., Notten, P.H.L., *J. Electrochem. Soc.*, **2013**, *160*, A3066.
(14) Prinz, F.B., *ECS Trans.*, **2008**, *16*, 15.
(15) Bakke, J.R., Pickrahn, K.L., Brennan, T.P., Bent, S.F., *Nanoscale* **2011**, *3*, 3482.
(16) van Delft, J.A., Garcia-Alonso, D., Kessels, W.M.M., *Semicond. Sci. Technol.,* **2012**, *27*, 074002.
(17) Dingemans, G., Kessels, W.M.M., *J. Vac. Sci. Technol. A,* **2012**, *30*, 040802.
(18) Naghavi, N., Abou-Ras, D., Allsop, N., Barreau, N., Bücheler, S., Ennaoui, A., Fischer, C.-H., Guillen, C., Hariskos, D., Herrero, J., Klenk, R., Kushiya, K., Lincot, D., Menner, R., Nakada, T., Platzer-Björkman, C., Spiering, S., Tiwari, A.N., Törndahl, T., *Prog. Photovoltaics Res. Appl.,* **2003**, *11*, 437.
(19) Choi, H., Nahm, C., Kim, J., Kim, C., Kang, S., Hwang, T., Park, B., *Curr. Appl. Phys.* **2013**, *13*, S2.
(20) Tien T.C., Pan F.M., Wang L.P., Tsai F.Y., Lin C., *J. Phys. Chem. C*, **2010**, *114*, 10048.
(21) Potscavage, W.J., Yoo, S., Domercq, B., Kippelen, B., *Appl. Phys. Lett.* **2007**, *90*, 253511.
(22) Jiang, X., Huang, H., Prinz, F.B., Bent, S.F., *Chem. Mater.* **2008**, *20,* 3897.
(23) Johansson, A.-C., Yang, R.B., Haugshøj, K.B., Larsen, J.V., Christensen, L.H., Thomsen, E.V., *Int. J. Hydrogen Energy* **2013**, *38*, 11406.
(24) Garcia-Alonso, D., Zardetto, V., Mackus, A.J.M., De Rossi, F., Verheijen, M.A., Brown, T.M., Kessels, W.M.M., Creatore, M., to be published.

CVD/ALD Precursors Packaged in Cylinders for Deposition Systems

For a complete list of CVD/ALD precursors packaged in cylinders for deposition systems, visit aldrich.com/ald.

Product Name	Acronym	Structure	Form	Prod. No.
Bis(ethylcyclopentadienyl)cobalt(II)	$(EtCp)_2Co$	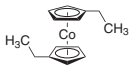	liquid	753076-10G
Bis(methyl-η^5–cyclopentadienyl)methoxymethyl-zirconium	ZrD-CO_4; ZRCMMM		liquid	725471-10G
Diethylzinc	DEZ; DEZn; Et_2Zn	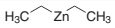	liquid	668729-25G
Tetrakis(diethylamido)titanium(IV)	TDEAT	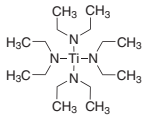	liquid	725536-10G
Tetrakis(dimethylamido)titanium(IV)	TDMAT	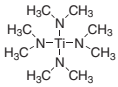	liquid	669008-25G
Tetrakis(dimethylamido)zirconium(IV)	TDMAZ	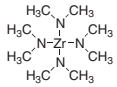	solid	669016-25G
Tetrakis(ethylmethylamido)zirconium(IV)	TEMAZ	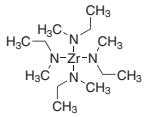	liquid	725528-10G
Titanium(IV) isopropoxide	TTIP	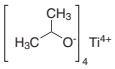	liquid	687502-25G
Titanium tetrachloride	TTC	$TiCl_4$	liquid	697079-25G
Triethylgallium	TEG; TEGa; Et_3Ga	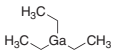	liquid	730726-10G
Trimethylaluminum	TMA		liquid	663301-25G
Trimethylgallium	TMG; TMGa; Me_3Ga		liquid	730734-10G
Trimethyl(methylcyclopentadienyl)platinum(IV)	$MeCpPtMe_3$	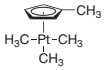	low-melting solid	697540-10G
Tris[*N,N*-bis(trimethylsilyl)amide]yttrium	YTDTMSA	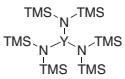	powder	702021-10G
Water	-	H_2O	liquid	697125-25ML
Zirconium(IV) *tert*-butoxide	ZTB	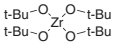	liquid	759554-25G

Vapor and Solution Deposition Precursors for Energy Applications

For a complete list of vapor and solution deposition precursors for energy applications, visit aldrich.com/mnel.

Batteries

Product Name	Structure	Purity	Form	Prod. No.
Aluminum acetylacetonate	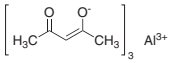	99.999% trace metals basis	solid powder	674753-5G 674753-25G
Aluminum isopropoxide	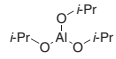	≥99.99% trace metals basis	solid powder and chunks	229407-10G 229407-50G 229407-250G
Aluminum tris(2,2,6,6-tetramethyl-3,5-heptanedionate)	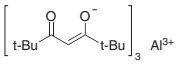	98%	solid	397288-5G
Bis(cyclopentadienyl)cobalt(II)		-	solid powder or crystals	339164-2G 339164-10G
Bis(ethylcyclopentadienyl)cobalt(II)	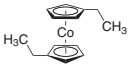	-	liquid	510645-1G
Bis(pentamethylcyclopentadienyl)cobalt(II)	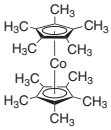	-	solid	401781-1G
Cobalt(II) acetate	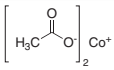	99.995% trace metals basis	solid crystals and lumps	399973-1G 399973-10G
Cobalt(III) acetylacetonate	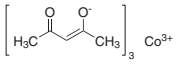	99.99% trace metals basis	granular powder or crystals	494534-5G 494534-25G
Cobalt(II) hexafluoroacetylacetonate hydrate	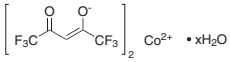	98%	solid powder or crystals	339695-5G
Lithium acetate		99.95% trace metals basis	powder or crystals	517992-100G
Lithium *tert*-butoxide		97%	powder and chunks	400173-25G 400173-100G
Lithium *tert*-butoxide solution		-	liquid	398209-50ML 398209-250ML
Lithium *tert*-butoxide solution		-	liquid	398195-50ML 398195-250ML
Lithium ethoxide	CH_3CH_2OLi	95%	powder and chunks	400203-5G 400203-25G
Lithium methoxide	CH_3OLi	98%	powder	344370-25G 344370-100G
Tetrakis(diethylamido)titanium(IV)	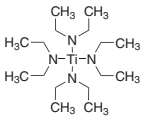	99.999% trace metals basis	liquid	469866-5G 469866-25G
Tetrakis(dimethylamido)titanium(IV)	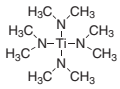	99.999%	liquid	469858-5G 469858-25G
Tetrakis(ethylmethylamido)titanium(IV)	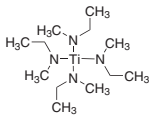	≥99.99%	liquid	473537-5G
Titanium(IV) *tert*-butoxide	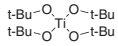	-	liquid	462551-25ML 462551-50ML

Product Name	Structure	Purity	Form	Prod. No.
Titanium(IV) diisopropoxidebis(2,2,6,6-tetramethyl-3,5-heptanedionate)	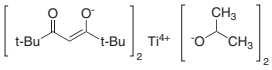	99.99%	solid	494143-5G
Titanium(IV) isopropoxide	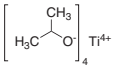	99.999% trace metals basis	liquid	377996-5ML 377996-25ML 377996-100ML
Triisobutylaluminum	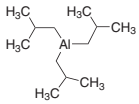	-	liquid	257206-100G 257206-500G 257206-1KG
Trimethylaluminum		97%	liquid	257222-100G
Tris(dimethylamido)aluminum(III)	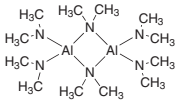	-	solid	469947-10G

Fuel Cells and Solar Cells

Product Name	Structure	Purity	Form	Prod. No.
Copper bis(6,6,7,7,8,8,8-heptafluoro-2,2-dimethyl-3,5-octanedionate)	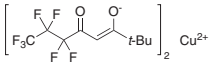	≥99.99% trace metals basis	solid	541761-1G 541761-5G
Copper bis(2,2,6,6-tetramethyl-3,5-heptanedionate)	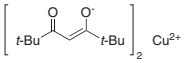	99%	solid	345083-1G
Gallium(III) acetylacetonate	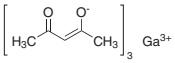	99.99% trace metals basis	solid	393541-5G 393541-25G
Indium(III) acetate hydrate	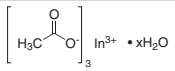	99.99% trace metals basis	powder and chunks	342378-5G 342378-25G
Indium(III) acetylacetonate	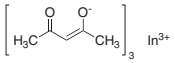	≥99.99% trace metals basis	solid	I3300-5G
Indium(III) isopropoxide solution	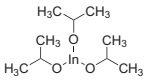	≥99% trace metals basis	liquid	760285-5ML
Tetrakis(dimethylamido)zirconium(IV)	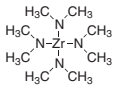	≥99.99%	solid	579211-5G
Tris(butylcyclopentadienyl)yttrium(III)	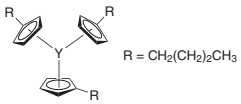	99.9% trace metals basis	liquid	524522-5ML
Tris(dimethylamido)gallium(III)	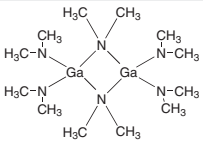	98%	solid	546534-5G
Yttrium(III) acetylacetonate hydrate	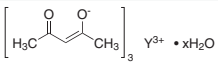	99.95% trace metals basis	powder or crystals	438790-5G
Yttrium(III) 2-ethylhexanoate	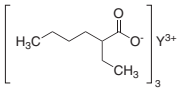	99.9% trace metals basis	powder or crystals	347086-10G
Yttrium(III) hexafluoroacetylacetonate dihydrate	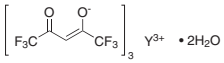	98%	powder or crystals	345601-5G

Fuel Cells and Solar Cells *(continued)*

Product Name	Structure	Purity	Form	Prod. No.
Yttrium 2-methoxyethoxide solution		-	liquid	771538-25G
Yttrium(III) tris(2,2,6,6-tetramethyl-3,5-heptanedionate)	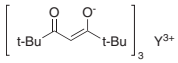	99.9% trace metals basis	solid	373826-1G
Zirconium(IV) *tert*-butoxide	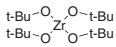	99.999% trace metals basis	liquid	560030-5G 560030-25G
Zirconium(IV) dibutoxide(bis-2,4-pentanedionate) solution	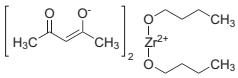	99.9% trace metals basis	liquid	771600-100G
Zirconium(IV) diisopropoxidebis(2,2,6,6-tetramethyl-3,5-heptanedionate)	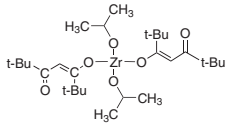	≥99.99%	solid	494151-25G
Zirconium(IV) 2-ethylhexanoate in mineral spirits	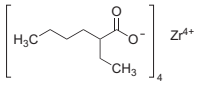	~6% Zr basis	liquid	768634-50G
Zirconium tetrakis(2,2,6,6-tetramethyl-3,5-heptanedionate)	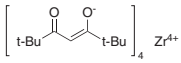	≥99.99%	solid	478865-5G 478865-25G

Sputtering Targets for Energy Applications

For a complete list of sputtering targets for energy applications, visit aldrich.com/pvd.

Product Name	Composition	Dimensions	Purity	Prod. No.
Aluminum	Al	diam. × thickness 3.00 × 0.125 in.	99.9995% trace metals basis	749036-1EA
Aluminum zinc oxide	Al_20_3/ZnO	diam. × thickness 3.00 × 0.125 in.	99.99% trace metals basis	752665-1EA
Chromium	Cr	diam. × thickness 3.00 × 0.125 in.	99.95% trace metals basis	749052-1EA
Gallium zinc oxide	ZnO/Ga_2O_3	diam. × thickness 3.00 × 0.125 in.	99.99% trace metals basis	752673-1EA
Indium oxide	In_2O_3	diam. × thickness 3.00 × 0.125 in.	99.99% trace metals basis	752649-1EA
Indium tin oxide	In_2O_3/SnO_2	diam. × thickness 3.00 × 0.125 in.	99.99% trace metals basis	752657-1EA
Indium zinc oxide	In_2O_3/ZnO	diam. × thickness 3.00 × 0.125 in.	99.99% trace metals basis	752703-1EA
Titanium	Ti	diam. × thickness 3.00 × 0.125 in.	99.995% trace metals basis	749044-1EA
Zinc	Zn	diam. × thickness 3.00 × 0.125 in.	99.995% trace metals basis	749060-1EA
Zinc oxide	ZnO	diam. × thickness 3.00 × 0.125 in.	99.99% trace metals basis	752681-1EA

Substrates for Thin Film Deposition

For a complete list of substrates for thin film deposition, visit aldrich.com/substrates.

Product Name	Composition	Dimensions	Orientation	Prod. No.
Aluminum oxide	Al_2O_3	L × W × thickness 10 × 10 × 0.5 mm	<0001>	634875-1EA 634875-5EA
Magnesium aluminate	MgO·Al_2O_3	L × W × thickness 10 × 10 × 0.5 mm	<100>	635073-1EA
Magnesium oxide	MgO	L × W × thickness 10 × 10 × 0.5 mm	<100>	634646-1EA
Silicon	Si	diam. × thickness 2 in. × 0.5 mm	<100>	646687-1EA 646687-5EA
	Si	diam. × thickness 3 in. × 0.5 mm	<100>	647535-1EA 647535-5EA
	Si	diam. × thickness 2 in. × 0.5 mm	<111>	647101-1EA 647101-5EA
Silicon dioxide	SiO_2	L × W × thickness 10 × 10 × 0.5 mm	<0001>	634867-5EA
Strontium titanate	$SrTiO_3$	L × W × thickness 10 × 10 × 0.5 mm	<110>	634670-1EA
Titanium(IV) oxide, rutile	TiO_2	L × W × thickness 10 × 10 × 0.5 mm	<001>	635057-1EA
	TiO_2	L × W × thickness 10 × 10 × 0.5 mm	<100>	635049-1EA

ALDRICH® Materials Science

Materials and Services for High-tech Applications

The Aldrich® Center of Excellence for Hard Materials provides a comprehensive range of high-purity products and custom services to suit the needs of academic and industrial researchers—from Alternative Energy and Advanced Electronics to Biomedical Applications. Materials expertise covers pure metals, alloys and metallurgical solids, salts, advanced ceramics, and complex oxides.

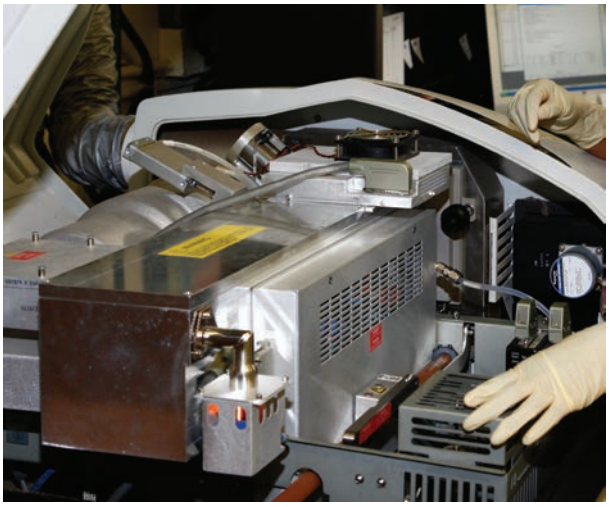

Capabilities include:

- Rare earth recovery and purification
- Purification of metals by distillation
- High temperature solid-state synthesis
- Beading of metals and salts
- High-purity and anhydrous salts
- Mechanochemical synthesis of inorganic and hybrid materials
- Synthesis and packaging under controlled/inert-gas atmosphere
- Full analytical suite including XRD, particle size analysis, ICP-MS/OES, DSC/TGA, elemental analysis, and NMR

Inquire about our custom capabilities at
HardMaterials@sial.com

Highly Efficient Nanoscale Inorganic Light Harvesters for Dye-sensitized Solar Cells

Nam-Gyu Park
School of Chemical Engineering and Department of Energy Science
Sungkyunkwan University, Suwon 440-746, Republic of Korea
Email: npark@skku.edu
Phone: +82-31-290-7241. Fax: +82-31-290-7272

Introduction

Since the first report of the low-cost dye-sensitized solar cell (DSSC) in 1991 by Gratzel and his coworker,[1] dye-sensitized solar cells (DSSC) has been regarded as one of the most promising photovoltaic technologies because of their transparent and colorful characteristics, as well as low cost. Unlike the semiconductor *p–n* junction-type solar cell, DSSC has been categorized as a liquid junction type because it contains a redox electrolyte. However, DSSC can also be fabricated as a solid-state structure by replacing the liquid electrolyte with solid hole conductors. DSSC is composed of a nanocrystalline TiO_2 film deposited on a fluorine-doped tin oxide (FTO) substrate, a redox electrolyte or a hole conductor, and a counter electrode. Light harvesters are adsorbed onto a TiO_2 surface to generate electrons and holes. Pt or carbon can be used as the counter electrode material for liquid junction-type device, and Au or Ag can be used as the counter electrode material for the solid-state devices. During the past two decades, substantial progress has been made. As a result, solar-to-electricity conversion efficiencies as high as 12% have been achieved using a 10-µm mesoporous TiO_2 film whose surface was sensitized with porphyrin dye and a cobalt redox electrolyte.[2] Meanwhile, solid-state DSSC was developed in 1998 by replacing the liquid electrolyte with 2,2′,7,7′-tetrakis(N,N-*p*-dimethoxy-phenylamino)-9,9′-spirobifluorene (spiro-MeOTAD) as a hole conductor.[3] However, the conversion efficiency was as low as 1%. To improve the efficiency, organic dyes with high absorption coefficients have been designed and synthesized for solid-state DSSC. Despite these efforts, no significant improvement has been made. Inorganic quantum dot materials, such as Sb_2S_3 (Aldrich Prod. Nos. 229466 and 244562) and CdSe (Aldrich Prod. No. 244600), have been applied as sensitizers, and show better efficiency than organic sensitizers.[4,5] A breakthrough technology in solid-state DSSC was made in 2012 by Park's group, where $CH_3NH_3PbI_3$ perovskite sensitizer adsorbed onto a 0.6-µm thick TiO_2 film delivered an efficiency of 9.7%.[6] Soon after our report, 15% efficiency was reported based on a perovskite sensitizer.[7] Progress in DSSC employing nanoscale inorganic sensitizers is presented here.

Importance of Mesoporous TiO_2 Film

In DSSC, among the three important components (mesoporous *n*-type oxide film, sensitizer, and redox electrolyte or *p*-type hole conductor), the mesoporous oxide film should be considered first because photovoltaic performance depends significantly on crystal phase, band structure, morphology, pore size, and porosity of the oxide layer. Differences in the crystal phase of the used TiO_2 film can lead to different photovoltaic performance although the same sensitizer and electrolyte are used. For example, anatase TiO_2 (Aldrich Prod. No. 637254) was found to be superior to rutile TiO_2 (Aldrich Prod. No. 637262).[8] Electron transport kinetics are influenced by nanoprticle packing structure, where the closely packed anatase TiO_2 film showed faster electron transport than the loosely packed rutile TiO_2 one.[8] In order to utilize incoming light more effectively, a bilayer structure composed of a light scattering overlayer on the nanocrystalline, semitransparent layer is proposed as better than a single layer comprised of TiO_2 nanoparticles (Aldrich Prod. Nos. 700347, 700355, and 700339). The scattering effect is expected to depend on the size, refractive index, and/or position of the scattering particle. The size-dependent scattering efficiency at the bilayer structure was studied, and light scattering was found to be related to wavelength-dependent light reflection.[9] Large TiO_2 particles with spherical shapes are normally used for the scattering layer. Although these large-sized particles play an important role in light scattering, such a low-surface-area scattering particle hardly offers any additional effect, such as electron generation, because dye adsorption is expected to be much less for large particles than for nanocrystalline TiO_2. To overcome this problem, bi-functional TiO_2 having a nano-embossed hollow spherical shape was developed, which was confirmed to be better than the simple large sized TiO_2.[10] Control of the porous structure in TiO_2 film is also important in terms of dye adsorption, transport of redox shuttle, and infiltration of the hole conductor. Selective positioning of three different dyes was realized by controlling pore size.[11] Compared to the iodide/iodine redox shuttle, pore size and porosity of a TiO_2 film is more critical for mass transport of larger redox shuttles such as cobalt complexes.[12] Thus, a well-organized mesoporous TiO_2 film is specifically required for high efficiency DSSC.

Solid-state DSSC Based on $CH_3NH_3PbI_3$ Perovskite Light Harvester

Solid-state DSSC is a kind of *pin* junction type, where the intrinsic (*i*) light harvester-adsorbed TiO_2 (*n*) is in contact with the *p*-type (*p*) hole transport material (HTM). **Figure 1** shows the cross-sectional SEM image of a real device. A blocking layer is deposited on an FTO glass to prevent direct contact between FTO and HTM. Mesoporous TiO_2 film forms on the blocking layer, where a submicrometer thickness is recommended for the perovskite sensitizer. Spiro-MeOTAD HTM material is infiltrated into the mesoporous film. A metal layer such as gold or silver is then deposited on top of the HTM layer.

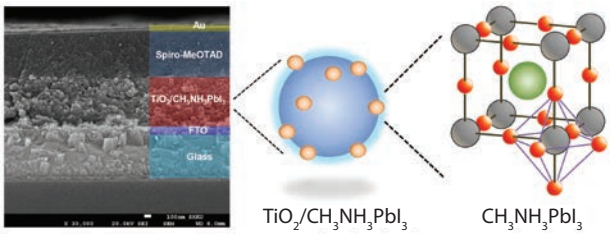

Figure 1. Solid-state DSSC structure showing (left) cross-sectional view of real device, (middle) perovskite $CH_3NH_3PbI_3$ adsorbed TiO_2 and (right) $CH_3NH_3PbI_3$ perovskite structure. Green, gray, and red spheres represent $CH_3NH_3^+$, Pb^{2+}, and I^-, respectively.

A breakthrough for the solid-state DSSC was made in 2012 using the organolead halide perovskite $CH_3NH_3PbI_3$, in which a PCE of 9.7% was demonstrated under the simulated AM1.5G one sun illumination.[6] The perovskite sensitizer can be deposited on the TiO_2 surface by either one-step[6] or two-step[7] coatings. For the one-step coating, CH_3NH_3I is first prepared by reacting CH_3NH_2 (Aldrich Prod. No. 295531) and HI (Aldrich Prod. No. 752851), which is mixed with PbI_2 (Aldrich Prod. No. 203602) in γ-butyrolactone (GBL) (Aldrich Prod. No. B103608) or dimethylformamide (DMF) (Sigma-Aldrich Prod. No. D158550). For the two-step coating, PbI_2 forms first on the TiO_2 surface, which is followed by dipping the PbI_2-coated TiO_2 film in the CH_3NH_3I solution. The perovskite solar cell also shows long-term stability. Two months later, higher efficiency was reported using a mixed halide perovskite, where a PCE of more than 10% was achieved using the $CH_3NH_3PbI_2Cl$ adsorbed Al_2O_3 layer.[13] Al_2O_3 used in this device acts simply as a scaffold layer, not as an electron accepting layer. Further improvement in PCE was achieved in 2013, where 12.3% was reported using the $CH_3NH_3PbI_3$ sensitizer and polytriarylamine (PTAA) (Aldrich Prod. No. 702471) HTM,[14] and the certified efficiency of 14.1% was reported.[2] Perovskite solar cells show very high photovoltage approaching or higher than 1 V, which is not generally observed from organic dye solar cells. In addition, high photocurrent can be achieved from the submicrometer-thick TiO_2 layer. The question is why organolead halide perovskite solar cells show extremely high photovoltaic performance. One reason is a high absorption coefficient, more than one order of magnitude higher for $CH_3NH_3PbI_3$ than N719 dye.,[15] Another important reason is the perovskite sensitizer has the ability to accumulate charges (**Figure 2**), which was confirmed by detection of capacitance measured by impedance spectroscopy.[16] Efficiency as high as 20% is realistically expected from the organometal halide perovskite solar cells because of the unique opto-electronic property of the perovskite sensitizer.[17]

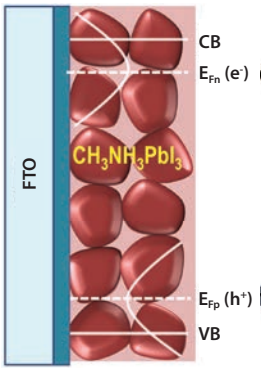

Figure 2. Schematic showing density of state, associated with charge accumulation, for the light harvesting perovskite $CH_3NH_3PbI_3$. The blocking layer is presented in between FTO and perovskite.

Quantum Dot-sensitized Solar Cell

Quantum dots (QDs, semiconductor nanocrystals) are one of the promising sensitizers for DSSC because of their high absorption coefficient, tunable band gap, and the possibility of multiple exciton generation (MEG). In order to utilize not only visible but also near infrared (NIR) light, low band gap QDs should be designed. Among the various low band gap QDs, PbS is one of the most intensively studied since it has a high absorption coefficient and a wide range of tunable band gap owing to its large Bohr exciton radius of 18 nm.[18] PbS QDs have been applied to DSSC, and a high PCE of 3.82% with photocurrent of 18.84 mA/cm^2 was reported.[19] However, the observed photocurrent was far below the theoretical value. Inefficient charge separation and collection, associated with electron injection and recombination, is argued to be the main drawback limiting the performance in PbS QDs. We have recently solved this problem by a doping method.[5] The successive ionic layer adsorption and reaction (SILAR) method was used to deposit QDs on the TiO_2 surface, where co-deposition of Pb and Hg ions led to Hg-doped PbS QDs. Compared to the bare PbS QDs, Hg-doped PbS QDs showed a much higher photovoltaic performance, especially a superb photocurrent approaching 30 mA/cm^2. From the analysis of the extended X-ray absorption fine structure (EXAFS) and femto-second laser dynamics, the significant improvement in optical property was found to be related to the structural change and the enhanced chemical bonding nature between Pb and S.

Figure 3 shows the I-V characteristics of a Hg-doped PbS QD-sensitized solar cell. Recently, we proposed a new technology to increase the number of QDs on the oxide surface by controlling surface charge through modification of solution pH.[20] The pH of the solution containing Pb^{2+} and Hg^{2+} was determined to be 3.2, where the TiO_2 surface was positively charged as this was lower than the point of zero charge (pH=6) for TiO_2. However, addition of triethanolamine (TEA) (Sigma-Aldrich Prod. No. 33729) changed the pH from 3.2 to 8.5, leading to a negatively charged surface. The amount of the adsorbed QDs increased from 2.3×10^4 μm^{-2} without TEA to 5.0×10^4 μm^{-2} with TEA because of strong interaction between the positive ions and the negative TiO_2 surface. Thanks to the significantly increased QD concentration in the given TiO_2 film, six-fold enhancement in photocurrent was realized by the surface charge control method. Apart from the PbS QD, several other quantum dots such as InP, CdS, CdSe, and Sb_2S_3 have been investigated as either sensitizer or *p*-type light harvester in a *p–n* junction solar cell. Since most of the inorganic nanocrystals exhibit much higher absorption coefficients than molecular sensitizers, QD materials are expected to be promising light harvesters for thin film solar cells.

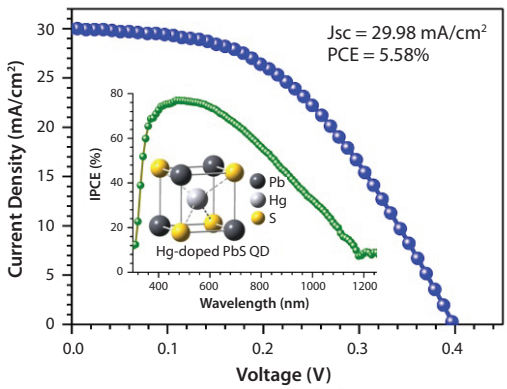

Figure 3. Photocurrent density-voltage curve for the Hg-doped PbS QD-sensitized solar cell. Inset shows the IPCE spectrum and local geometry of Hg-doped PbS QDs.

Summary and Perspective

Inorganic sensitizers such as organometal halide perovskites and metal chalcogenides were reviewed. Methylammonium lead halide perovskites made a breakthrough in the dye-sensitized solar cell field. Since long-term stability was confirmed and the perovskite could form on an oxide surface within few seconds, commercialization of perovskite solar cell is likely. In addition, low-cost high efficiency solar cell technology is expected from perovskite solar cells since a PCE of 20% is realistically possible. For QDs, panchromatic absorption from visible to near IR is attainable by tuning the bandgap through quantum size effect, which can lead to extremely high photocurrent density. The challenging task of the future will be combining perovskite and NIR-absorbing QDs into super high efficiency technologies.

Acknowledgments

This work was supported by the National Research Foundation of Korea (NRF) grants funded by the Ministry of Science, ICT & Future Planning (MSIP) of Korea, under contracts no. NRF-2010-0014992, NRF-2012M1A2A2671721, NRF-2012M3A6A7054861 (Nano Material Technology Development Program) and NRF-2012M3A6A7054861 (Global Frontier R&D Program on Center for Multiscale Energy System).

References

(1) O'Regan, B.; Gratzel, M., *Nature* **1991**, *353*, 737.
(2) Yella, A.; Lee, H.-W.; Tsao, H. N.; Yi, C.; Chandiran, A. K.; Nazeeruddin, Md. K.; Diau, E. W.-G.; Yeh, C.-Y.; Zakeeruddin, S. M.; Grätzel, M., *Science* **2011**, *334*, 629.
(3) Bach, U.; Lupo, D.; Comte, P.; Moser, J. E.; Weissörtel, F.; Salbeck, J.; Spreitzer, H.; Grätzel, M. *Nature* **1998**, *395*, 583.
(4) Chang, J. A.; Im, S. H.; Lee, Y. H.; Kim, H.-j.; Lim, C.-S.; Heo, J. H.; Seok, S. I. *Nano Lett.* **2012**, *12*, 1863.
(5) Lee, J.-W.; Son, D.-Y.; Ahn, T. K.; Shin, H.-W.; Kim, I. Y.; Hwang, S.-J.; Ko, M. J.; Sul, S.; Han, H.; Park, N.-G. *Sci. Rep.* **2013**, *3*, 1050.
(6) Kim, H.-S.; Lee, C.-R.; Im, J.-H.; Lee, K.-B.; Moehl, T.; Marchioro, A.; Moon, S.-J.; Humphry-Baker, R.; Yum, J.-H.; Moser, J. E.; Grtazel, M.; Park, N.-G. *Sci. Rep.* **2012**, *2*, 591.
(7) Burschka, J.; Pellet, N.; Moon, S.-J.; Humphry-Baker, R.; Gao, P.; Nazeeruddin, M. K.; Grätzel, M. *Nature* **2013**, *499*, 316.
(8) Park, N.-G.; van de Lagemaat, J.; Frank, A. J. *J. Phys. Chem. B* **2000**, *104*, 8989.
(9) Koo, H.-J.; Park, J.; Yoo, B.; Yoo, K.; Kim, K.; Park, N.-G. *Inorg. Chim. Acta* **2008**, *361*, 677.
(10) Koo, H.-J.; Kim, Y. J.; Lee, Y. H.; Lee, W. I.; Kim, K.; Park, N.-G. *Adv. Mater.* **2008**, *20*, 195.
(11) Lee, K.; Park, S. W.; Ko, M. J.; Kim, K. Park, N.-G. *Nat. Mater.* **2009**, *8*, 665.
(12) Kim, H.-S.; Ko, S.-B.; Jang, I.-H.; Park, N.-G. *Chem. Commun.* **2011**, *47*, 12637.
(13) Lee, M. M.; Teuscher, J.; Miyasaka, T.; Murakami, T. N.; Snaith, H. J. *Science* **2012**, *338*, 643.
(14) Noh, J. H.; Im, S. H.; Heo, J. H.; Mandal, T. N.; Seok, S. I. *Nano Lett.* **2013**, *13*, 1764.
(15) Im, J.-H.; Lee, C.-R.; Lee, J.-W.; Park, S.-W.; Park, N.-G. *Nanoscale* **2011**, *3*, 4088.
(16) Kim, H.-S.; Mora-Sero, I.; Gonzalez-Pedro, V.; Fabregat-Santiago, F.; Juarez-Perez, E. J.; Park, N.-G.; Bisquert, J. *Nat. Commun.* **2013**, *4*, 2242.
(17) Park, N.-G. *J. Phys. Chem. Lett.* **2013**, *4*, 2423.
(18) Scholes, G. D.; Rumbles, G. *Nat. Mater.* **2006**, *5*, 683.
(19) Zhou, N. *et al. Electrochem. Commun.* **2012**, *20*, 97.
(20) Lee, J.-W.; Hong, J.-D.; Park, N.-G. *Chem. Commun.* **2013**, *49*, 6448.

Core-Type Quantum Dots

For a complete list of core-type quantum dots, visit aldrich.com/quantumdots.

PbS

Product Name	Description	Fluorescence Emission	Prod. No.
PbS core-type quantum dots	4 x 10 mg/mL in toluene kit, oleic acid coated	λ_{em} = 1000-1600 nm	790494-1KT
	10 mg/mL in toluene oleic acid coated	λ_{em} = 1000 nm	747017-10ML
	10 mg/mL in toluene oleic acid coated	λ_{em} = 1200 nm	747025-10ML
	10 mg/mL in toluene oleic acid coated	λ_{em} = 1400 nm	747076-10ML
	10 mg/mL in toluene oleic acid coated	λ_{em} = 1600 nm	747084-10ML

CdTe

Product Name	Description	Fluorescence Emission	Prod. No.
CdTe core-type quantum dots	powder, COOH functionalized	λ_{em} = 510 nm	777986-10MG 777986-25MG
	powder, COOH functionalized	λ_{em} = 520 nm	777935-10MG 777935-25MG
	powder, COOH functionalized	λ_{em} = 570 nm	777943-10MG 777943-25MG
	powder, COOH functionalized	λ_{em} = 610 nm	777951-10MG 777951-25MG
	powder, COOH functionalized	λ_{em} = 710 nm	777978-10MG 777978-25MG
	powder, COOH functionalized	λ_{em} = 770 nm	777994-10MG 777994-25MG

CdSe and CdS

Product Name	Description	Particle Size	Fluorescence Emission	Prod. No.
Lumidot™ CdS, 380 core-type quantum dots	5 mg/mL in toluene	1.6 - 1.8 nm	λ_{em} = 370-390 nm	662429-10ML
Lumidot™ CdS, 460 core-type quantum dots	5 mg/mL in toluene	4.0 - 5.4 nm	λ_{em} = 450-470 nm	662372-10ML

Product Name	Description	Particle Size	Fluorescence Emission	Prod. No.
Lumidot™ CdSe, 480 core-type quantum dots	5 mg/mL in toluene	2.1 - 2.3 nm	λ_{em} = 475-485 nm	662356-10ML
Lumidot™ CdSe, 520 core-type quantum dots	5 mg/mL in toluene	2.4 - 2.6 nm	λ_{em} = 515-525 nm	662437-10ML
Lumidot™ CdSe, 560 core-type quantum dots	5 mg/mL in toluene	3.0 - 3.5 nm	λ_{em} = 555-565 nm	662445-10ML
Lumidot™ CdSe, 590 core-type quantum dots	5 mg/mL in toluene	4.0 - 4.3 nm	λ_{em} = 585-595 nm	662607-10ML
Lumidot™ CdSe, 610 core-type quantum dots	5 mg/mL in toluene	4.7 - 5.2 nm	λ_{em} = 605-615 nm	662488-10ML

Core-Shell Type Quantum Dots

For a complete list of core-shell type quantum dots, visit aldrich.com/quantumdots.

InP/ZnS

Product Name	Description	Fluorescence Emission	Prod. No.
InP/ZnS-5 Quantum dots kit	5 × 5mg/mL in toluene, stabilized with oleylamine ligands	λ_{em} = 530-650 nm	777285-1KT
InP/ZnS quantum dots	5 mg/mL in toluene, stabilized with oleylamine ligands	λ_{em} = 530 nm	776750-5ML
	5 mg/mL in toluene, stabilized with oleylamine ligands	λ_{em} = 560 nm	776793-5ML
	5 mg/mL in toluene, stabilized with oleylamine ligands	λ_{em} = 590 nm	776769-5ML
	5 mg/mL in toluene, stabilized with oleylamine ligands	λ_{em} = 620 nm	776777-5ML
	5 mg/mL in toluene, stabilized with oleylamine ligands	λ_{em} = 650 nm	776785-5ML

CdSe/ZnS

Product Name	Description	Fluorescence Emission	Prod. No.
CdSe/ZnS core-shell type quantum dots	stabilized with octadecylamine ligands, solid	λ_{em} = 520 nm	748021-10MG 748021-25MG
	stabilized with octadecylamine ligands, solid	λ_{em} = 540 nm	748056-25MG 748056-10MG
	stabilized with octadecylamine ligands, solid	λ_{em} = 560 nm	748080-25MG 748080-10MG
	stabilized with octadecylamine ligands, solid	λ_{em} = 580 nm	748129-10MG 748129-25MG
	stabilized with octadecylamine ligands, solid	λ_{em} = 600 nm	748099-25MG 748099-10MG
	stabilized with octadecylamine ligands, solid	λ_{em} = 620 nm	790192-25MG 790192-10MG
	stabilized with octadecylamine ligands, solid	λ_{em} = 630 nm	790206-25MG 790206-10MG

Alloyed Quantum Dots

For a complete list of alloyed quantum dots, visit aldrich.com/quantumdots.

Product Name	Description	Fluorescence Emission	Prod. No.
CdSeS/ZnS alloyed quantum dots kit	5 × 1 mg/mL in toluene, diameter 6 mm particle size 5.5 - 6.5 nm	λ_{em} = 490-665 nm	753823-1KT
CdSeS/ZnS alloyed quantum dots	1 mg/mL in toluene, diameter 6 nm	λ_{em} = 450 nm	753742-5ML 753742-25ML
	1 mg/mL in toluene, diameter 6 nm	λ_{em} = 490 nm	753750-5ML 753750-25ML
	1 mg/mL in toluene, diameter 6 nm	λ_{em} = 525 nm	753769-5ML 753769-25ML
	1 mg/mL in toluene, diameter 6 nm	λ_{em} = 540 nm	753777-5ML 753777-25ML
	1 mg/mL in toluene, diameter 6 nm	λ_{em} = 575 nm	753785-5ML 753785-25ML
	1 mg/mL in toluene, diameter 6 nm	λ_{em} = 630 nm	753793-5ML 753793-25ML
	1 mg/mL in toluene, diameter 6 nm	λ_{em} = 665 nm	753807-5ML 753807-25ML
	1 mg/mL in H_2O, diameter 6 nm, COOH functionalized	λ_{em} = 490 nm	754226-1ML 754226-5ML
	1 mg/mL in H_2O, diameter 6 nm, COOH functionalized	λ_{em} = 525 nm	753831-1ML 753831-5ML
	1 mg/mL in H_2O, diameter 6 nm, COOH functionalized	λ_{em} = 540 nm	753866-1ML 753866-5ML
	1 mg/mL in H_2O, diameter 6 nm, COOH functionalized	λ_{em} = 575 nm	753874-1ML 753874-5ML
	1 mg/mL in H_2O, diameter 6 nm, COOH functionalized	λ_{em} = 630 nm	753882-1ML 753882-5ML
	1 mg/mL in H_2O, diameter 6 nm, COOH functionalized	λ_{em} = 665 nm	753890-1ML 753890-5ML

Lead Precursors for Synthesis of Organolead Halides

For a complete list of lead precursors for synthesis of organolead halides, visit aldrich.com/periodic.

Product Name	Composition	Purity	Form	Prod. No.
Lead(II) acetate trihydrate	$Pb(CH_3CO_2)_2 \cdot 3H_2O$	≥99.99% trace metals basis	solid	467863-50G 467863-250G
Lead(II) bromide	$PbBr_2$	99.999%	beads	460583-1G
Lead(II) bromide	$PbBr_2$	99.999% trace metals basis	powder	398853-5G
Lead(II) carbonate	$PbCO_3$	≥99.99% trace metals basis	powder and chunks	335169-25G
Lead(II) carbonate basic	$(PbCO_3)_2 \cdot Pb(OH)_2$	-	powder	243582-100G 243582-2.5KG
Lead(II) chloride	$PbCl_2$	99.999%	beads	449865-5G
Lead(II) iodide	PbI_2	99.999% trace metals basis	beads	554359-5G
Lead(II) iodide	PbI_2	99.999% trace metals basis	solid	203602-50G
Lead(II) sulfate	$PbSO_4$	99.995% trace metals basis	powder and chunks	254258-10G 254258-50G

Titanium Oxide Nanomaterials

For a complete list of titanium oxide nanomaterials, visit aldrich.com/nanomaterials.

Product Name	Description	Purity	Form	Prod. No.
Titanium(IV) oxide	particle size 21 nm (TEM) surface area 35-65 m^2/g (BET)	≥99.5% trace metals basis	nanopowder	718467-100G
Titanium(IV) oxide, anatase	particle size <25 nm spec. surface area 45-55 m^2/g	99.7% trace metals basis	nanopowder	637254-50G 637254-100G 637254-500G
Titanium(IV) oxide, mixture of rutile and anatase	particle size <50 nm (XRD) particle size <100 nm (BET)	99.5% trace metals basis	nanopowder	634662-25G 634662-100G
Titanium(IV) oxide, mixture of rutile and anatase	particle size ~21 nm (primary particle size of starting nanopowder) particle size <250 nm (DLS) BET surf. area 50 m^2/g (BET surface area of starting nanopowder)	99.9% trace metals basis	nanoparticles paste	700355-25G
Titanium(IV) oxide, mixture of rutile and anatase	particle size <150 nm (DLS) particle size ~21 nm (primary particle size of starting nanopowder)	99.9% trace metals basis	dispersion nanoparticles	700347-25G 700347-100G
Titanium(IV) oxide, mixture of rutile and anatase	particle size ~15 nm (primary particle size of starting nanopowder) particle size <100 nm (DLS) BET surf. area 90 m^2/g (BET surface area of starting nanopowder)	99.9% trace metals basis	dispersion nanoparticles	700339-100G
Titanium(IV) oxide, rutile	particle size <100 nm spec. surface area 130-190 m^2/g	99.5% trace metals basis	nanopowder	637262-25G 637262-100G 637262-500G

ALDRICH® Materials Science

Materials for Thermoelectric Applications

High-purity Materials for Your Research Needs

Aldrich® Materials Science offers high-purity metal chalcogenides and silicides suitable for thermoelectric applications or choose from our broad selection of percursors to fabricate your own thermoelectric material.

We continue to expand our portfolio of thermoelectric materials to include new advanced materials.

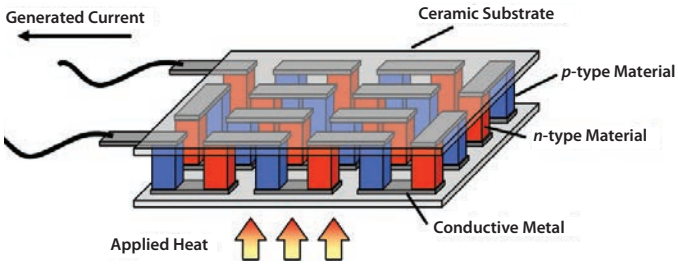

Thermoelectric Materials

Product Name	Linear Formula	Description	Purity	Prod. No.
Magnesium silicide	Mg_2Si	3–14 mm, pieces	99.7%, trace metals basis	752630
Iron disilicide	$FeSi_2$	–20 mesh, powder	99.9%, trace metals basis	752622
Molybdenum disilicide	$MoSi_2$	particle size 7.5 µm, powder	≥99.8%, trace metals basis	752290
Zinc antimonide	Zn_4Sb_3	–80 mesh, powder	99.9%, trace metals basis	745995
Bismuth antimonide	BiSb	–80 mesh, powder	99.9%, trace metals basis	745804
Bismuth antimony telluride	$BiSb_3Te_6$	beads	99.99%, trace metals basis	752509
Lead selenide telluride	Pb_2SeTe	–80 mesh, powder	99.9%, trace metals basis	745812
Bismuth(III) telluride	Bi_2Te_3	beads	99.995%, trace metals basis	751421
Antimony(III) telluride	Sb_2Te_3	beads	≥99.99%, trace metals basis	740993
Lead(II) telluride	PbTe	powder	99.998%, trace metals basis	254266

Precursors for Thermoelectric Materials Fabrication

Product Name	Description	Purity	Prod. No.
Bismuth	1–5 mm, beads	99.999%, trace metals basis	452386
	4–30 mesh, shot	99.9%, trace metals basis	265470
	~100 mesh, powder	≥99.99%, trace metals basis	264008
Antimony	1–5 mm, beads	99.999%, trace metals basis, low oxide	452343
	~100 mesh, powder	99.5%, trace metals basis	266329
Tellurium	ingot	99.999%, trace metals basis	263311
	pieces	99.999%, trace metals basis	204544
	~200 mesh, powder	99.8%, trace metals basis	266418
Selenium	<5 mm, pellets	≥99.999%, trace metals basis	204307
	~100 mesh, powder	99.99%, trace metals basis	229865

For a complete list of thermoelectric materials, visit
aldrich.com/thermoelectrics

ALDRICH®
Materials Science

Materials to Drive Innovation

Across a Variety of Applications

Energy

Electrode and electrolyte materials for batteries, fuel cells; hydrogen storage materials including MOFs; phosphors; thermoelectrics; nanomaterials; precursors for nanomaterials and nanocomposites

Biomedical

Materials for bone and tissue engineering: nanoclays, PEGs, biodegradable and natural polymers; functionalized nanoparticles; block copolymers and dendrimers

Electronics

Nanowires; printed electronics inks and pastes; materials for OPV, OFET, OLED; nanodispersions; CNTs and graphene; precursors for PVD, CVD, and sputtering

Gold nanoparticle dispersions:

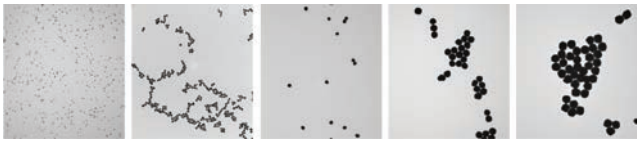

Find more information on our capabilities at
aldrich.com/matsci

PVS
81264-515940
11-2013